RADIAL DIFFUSION COEFFICIENT FOR COUNTER-PASSING MeV IONS IN THE TFTR TOKAMAK

S.J. ZWEBEN, R.L. BOIVIN, C.-S. CHANG,
G.W. HAMMETT, H.E. MYNICK
Princeton Plasma Physics Laboratory,
Princeton University,
Princeton, New Jersey,
United States of America

ABSTRACT. The radial diffusion coefficient for confined counter-passing MeV ions is evaluated in a new way, using measurements of escaping D–D fusion products. A class of passing ions near the plasma centre is measured whose orbits could eventually diffuse across their passing/trapped boundary, resulting in unconfined trapped orbits which can be detected at the plasma wall. The analysis indicates that the passing MeV ion diffusion coefficient D is smaller than ≈ 0.1 m^2/s, which is small compared to the thermal diffusivities of ≈ 1 m^2/s for these plasmas. The same experiment and analysis should be applicable to alpha particles in D–T plasmas.

1. INTRODUCTION

Confinement studies of MeV ions will play an important role in the research required to achieve burning plasmas in tokamaks [1, 2], since any significant radial transport of MeV alpha particles will affect the heating rate or heating profiles of these plasmas. Because the energy, gyroradius and collisionality of these MeV ions are very different from those of the background plasma, their transport rates *cannot* be assumed to be equal to those of the bulk plasma ions. Note that the desired confinement time for 3.5 MeV alphas is set by their thermalization time $\tau_{th,\alpha}$, which can be up to ≈ 1 s for the steady state phase of ITER, requiring a diffusion coefficient D < 0.5 m^2/s. This is equivalent to more than 100 000 alpha particle transits of the torus.

1.1. Basic physics

The are several distinct physical mechanisms which can lead to radial transport of MeV ions in a tokamak [3]. The simplest mechanism is first-orbit loss, which causes some fraction of the alphas to hit the wall within $\approx 10^{-6}$ s of their birth owing to their finite banana width. Globally, the first-orbit loss is >20% for plasma currents of <1 MA, but it should become negligible in reactor grade plasmas with >10 MA. A more subtle (but still predictable) loss mechanism is due to toroidal magnetic field (TF) ripple, which, even at 10 MA, can cause about 1–5% of the alphas to be lost owing to a random step at the banana tips of the trapped alphas [4, 5]. A third transport mechanism is large scale MHD activity, which in TFTR has already been seen to cause periodic MeV ion loss in phase with the usual m = 1–4 magnetic oscillations [6]. This MHD induced loss may be due either to the internal 'ripple' affecting trapped ions [3] or to the radial magnetic fields affecting the confined passing ions near the passing/trapped boundary [7].

The present paper concerns the search for a fourth possible loss mechanism, namely that due to small scale turbulence (i.e. fluctuations with $k_{pol}\rho_i \approx 1$ or $n \gg 1$), which could cause a radial diffusive loss of MeV ions. In this experiment, the radial transport of these MeV ions is inferred using a new technique by which the internal diffusion rate of confined counter-passing MeV ions can be found from the rate of MeV ion loss across the passing/trapped boundary, as measured by a detector of unconfined trapped ions at the vessel wall. These experiments are conducted with plasmas in which the coherent MHD induced loss is negligible, and we use a detector position at which the TF ripple loss should be absent. Thus, the focus of the analysis is to separate a possible diffusive loss from the expected first-orbit loss and thereby estimate the radial diffusion rate for this class of confined MeV ions.

Note that this technique is useful only for ions with large banana widths such as fusion products naturally produced by D–D fusion reactions, namely 1 MeV tritons and 3 MeV protons, one of each of which is created for every 2.5 MeV neutron. Both of these

MeV ions have initial toroidal gyroradii of about 0.05 m, i.e. about ten times that of thermal ions, and so have trapped particle orbits which can intersect the wall at the usual TFTR plasma currents of 1–2 MA.

For TFTR, the D–D reaction rates of $\approx 10^{16}$ neutrons/s produce a confined MeV ion population of $n_{MeV}/n_e < 10^{-4}$, assuming classical collisional slowing down over $\tau_s \approx 0.4$ s (average 1/e energy decay time for tritons and protons). Therefore, in the present experiment these D–D produced MeV ions constitute a non-perturbing and non-heating 'test ion' population. However, future TFTR experiments with D–T alphas will produce an ≈ 100 times larger MeV ion population, at which stage the collective instability and heating effects of the MeV ions may become significant. The study of alpha particle diffusion under these more reactor relevant conditions will be one of the main goals of these first D–T experiments [1]. The present experiment can be repeated in D–T plasmas to search for such collective alpha particle effects in TFTR.

1.2. Review of previous MeV ion experiments

Previous measurements of MeV ion loss in TFTR [6] have been compared only with the simple first-orbit loss model, without considering the possible effects of diffusion on the results. The present experimental results are quite similar to those found previously for MHD quiescent plasmas, but the analysis here is new and focuses on possible diffusive effects.

Previous triton burnup measurements in TFTR have recently been re-analysed with an improved time and space dependent burnup code [8]. The burnup fraction in TFTR supershots was about 0.5 times the classically expected value, which was shown to be consistent with a global triton confinement time of ≈ 0.5 s or a global triton diffusion coefficient of $D \approx 0.1$ m^2/s [9]. Note that TF ripple loss and/or MHD induced loss might be contributing to this anomalously low burnup.

Recent measurements of MeV ion diffusion have also been made in JET, using both the burnup of 1 MeV tritons [10] and the stored energy of MeV ion tails generated by minority heating in the ion cyclotron range of frequencies (ICRF) [11]. In both cases the inferred upper limit for the MeV ion diffusion coefficient was fairly low, i.e. $D \approx 0.1$–0.2 m^2/s, implying a global MeV ion confinement long enough for complete alpha thermalization in the D–T phase of JET. However, exceptions to this good confinement were noted for plasmas with large MHD activity and large sawtooth crashes.

Loss of the superthermal (but sub-MeV) ions used for auxiliary plasma heating in tokamaks has generally not been noticed, except during large scale MHD activity such as fishbones, although a quantitative measure of the diffusion coefficient has only rarely been obtained. Very low particle diffusion rates of $D < 0.1$ m^2/s have been estimated for ≈ 100 keV circulating beam ions in TFTR using charge exchange measurements [9, 12], and a similarly low diffusion rate was recently inferred for radiofrequency (RF) tail ions in TFTR [13].

1.3. Other relevant alpha particle studies

A general theory of MeV 'test ion' diffusion caused by small scale electromagnetic or electrostatic turbulence has been developed by White and Mynick [3] and Mynick and Duvall [14]. The basic result is that MeV ions with a large gyroradius ρ_{MeV} and banana width Δ_{MeV} should have a radial diffusion coefficient D_{MeV} lower than that of thermal ions, D_{slow}, by an 'orbit averaging' factor Λ, i.e.

$$D_{MeV} \approx \langle J_0^2(k_\perp \rho_{MeV}) J_0^2(k_\perp \Delta_{MeV}) \rangle \, D_{slow} \equiv \Lambda D_{slow} \quad (1)$$

where the factor Λ, involving the Bessel functions J_0, can be roughly approximated as

$$D_{MeV} \approx (1/k_\perp \rho_{MeV})\,(1/k_\perp \Delta_b) D_{slow} \quad (2)$$

For alpha particles in TFTR, in the presence of turbulence with $k_\perp \rho_i \approx 1$, MeV ion diffusion should be lower than thermal ion diffusion by a factor of $> 10^4$, given the same turbulence [7]. Thus, the expected turbulent diffusion rate for MeV ions in TFTR is very small, $D \approx 10^{-4}$ m^2/s, which is even less than the neoclassically expected value, $D \approx (r/R)\rho_{pol}^2 \nu_s \approx 0.04$ m^2/s [15] (see also Section 5.1).

2. EXPERIMENTAL SET-UP

2.1. Basic idea

The basic idea for this experiment is illustrated in Fig. 1. Fusion product ions are created inside the plasma and initially follow orbits which depend on their minor radius r at birth, their birth energy E_0 and their magnetic moment μ. The objective of the experiment is to distinguish between particles which might be lost owing

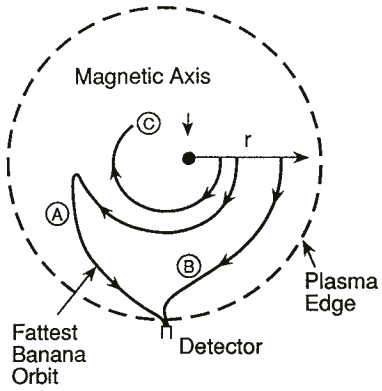

FIG. 1. Three guiding centre orbits for 1 MeV tritons (or 3 MeV protons) at 1.8 MA in TFTR, each of which can lead to loss to the detector at the bottom of the vessel. Orbit A is the fattest banana orbit, which represents the first-orbit loss from the region nearest the plasma centre. Orbit B represents a first-orbit loss from the largest detectable magnetic moment μ, which enters the detector at a larger pitch angle than does orbit A. Orbit C is a confined counter-passing orbit with the same values of μ and E as orbit A. Orbit C can diffuse radially until it mirrors, after which it is lost on the same trajectory as orbit A.

to any 'anomalous' radial diffusion and ions which are lost 'classically' on their first orbits.

Orbits such as those indicated by A and B in Fig. 1 correspond to first-orbit loss, i.e. the orbits are 'mirrored' by the 1/R toroidal magnetic field and almost immediately hit the bottom of the vessel. For a given detector location, these orbits were identified by the Lorentz orbit code ORBIT [16] which traces particles 'backward in time' from the detector into the plasma. Here, ions in orbits A and B enter the detector at their birth energy E_0, but have different values of μ. Orbit A is the 'fattest banana' orbit for this detector location and this energy, i.e. it is the loss orbit which has its banana tip closest to the midplane and so it passes closest to the banana centre [6]. Orbit B is the loss orbit with the largest measurable magnetic moment for this detector.

In contrast, counter-passing ions such as those in orbit C, which are born with the same μ and E_0 as those in orbit A, but at a smaller minor radius, should, in the absence of diffusion, remain confined on nearly the same orbit until they are thermalized. However, if a particle that is initially confined on orbit C has a rapid radial diffusion which brings its minor radius out to that of orbit A without a significant energy loss or change of μ, then it should also become trapped and lost to the detector along the same fattest banana trajectory as that of orbit A (the inclusion of classical energy loss during diffusion only slightly increases the minor radius at which the orbit is mirrored).

Thus, the qualitative signatures of diffusion are all associated with a loss near the passing/trapped boundary, as opposed to first-orbit loss which is normally distributed over a range of μ and r. These signatures are clarified and quantified in Section 3.

Note that the orbit characteristics illustrated in Fig. 1 were drawn for D–D fusion product ions at birth energy for the 1.8 MA TFTR plasma used in this experiment, which has a major radius $R_0 = 2.6$ m, a minor radius $a = 0.95$ m, a toroidal field on axis $B_0 = 3.7$ T and a Shafranov shift of the magnetic axis of ≈ 0.15 m. Similar drawings for low current TFTR plasmas (i.e. < 1 MA) show the fattest banana orbit passing very close to the plasma centre, with a correspondingly larger region of first-orbit loss and a smaller region of confined counter-passing ions (see Section 4). In this case, the signatures of diffusion should be qualitatively similar but quantitatively less significant.

Roughly speaking, a significant fraction of the internal confined counter-passing MeV ions should be lost when $D \approx r_{fb}^2/4\tau_{sE}$, where r_{fb} is the typical radius of the fattest banana orbit and τ_{sE} is the time over which MeV ions are observable (which is close to an energy e-folding time). For a typical 1.8 MA TFTR plasma, $r_{fb} = 0.5$ m and $\tau_{sE} \approx 0.4$ s, implying that a significant diffusive loss should occur at $D \approx 0.1$ m^2/s. Note that more precise evaluations of the diffusive loss depend on the profile shape of the MeV ion source and on the size and the magnetic moment of the fattest banana orbit, as discussed in Section 3.

2.2. MeV ion detector

The detector shown schematically in Fig. 2 consists of a 0.025 m × 0.025 m ZnS(Ag) scintillator screen inside a light-tight box. This detector is identical with that used for previous measurements in TFTR, as described in Ref. [6].

This detector is designed to disperse the various possible ion gyroradii ρ along one dimension of the scintillator screen (similarly to a magnetic spectrometer) and the various possible ion pitch angles χ across the other dimension. Here we define for convenience the orbit's pitch angle χ at the detector with respect to the local toroidal field such that $\cos\chi = v_\parallel/v_0$, where $v_\parallel$ is the ion velocity along the toroidal magnetic field B (i.e. $\chi = 0°$ corresponds to an ion orbit directed along B_0 and $\chi = 90°$ corresponds to an ion orbit perpendicular to B_0 at the detector). The two quantities ρ and χ are sufficient to define the ion energy and magnetic moment

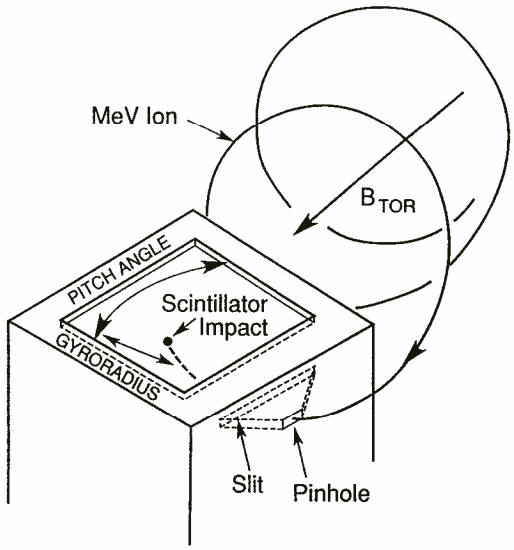

FIG. 2. Detector geometry showing the mechanism of pitch angle and energy resolution. Ions with gyroradii $\rho \approx 0.02$–0.11 m approach the detector on helical orbits, enter the front pinhole aperture and are dispersed in the gyroradius direction by the slit aperture (as in a magnetic spectrometer). The orbit pitch angle χ (measured here with respect to the TF) is resolved from its impact position along the direction of B. The scintillator screen is 0.025 m × 0.025 m and is viewed from below with lenses and fibre optics.

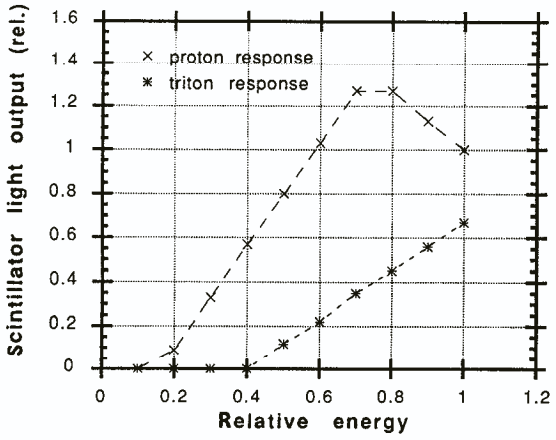

FIG. 3. Detector sensitivities versus incident ion energy (before passage through the foil) for tritons and protons. Low energy tritons (<0.4 MeV) do not pass the 3 μm aluminium foil, while high energy protons (>2.5 MeV) pass through the scintillator without depositing their full energy. These curves are based on results from a calibration made using a D–D generator [17]. The ^{3}He D–D fusion product is blocked by the foil.

(given the ion species) and hence to define the trajectory of the escaping ion for a specified magnetic geometry.

The 2-D images of the scintillator light emission (400–500 nm) are optically coupled through a lens and a coherent fibre bundle to an intensified video camera for analysis. The coherent fibre bundle used in the present experiment was made of improved low-loss quartz fibres instead of plastic fibres as used previously [6], but was still a 50 × 50 array of 250 μm fibres.

For these diffusion experiments it is necessary to model the response of this detector for various MeV ion energies. A new calibration of the MeV ion sensitivity of the ZnS(Ag) scintillators was made using a laboratory ion beam source of D–D fusion products [17]. When a 3 μm aluminium foil filter was used (as it was in the TFTR detector) the total light output for 1 MeV tritons was approximately two thirds of that of 3 MeV protons, since the effective scintillator thickness (at $\approx 75°$ to normal incidence) is somewhat smaller than the range of 3 MeV protons. Thus, the relative 3 MeV proton response is larger than was assumed previously on the basis of a simplified energy deposition calculation [6].

When the incident ion energies were decreased by using additional foils, the measured scintillator repsonse varied approximately as shown in Fig. 3 [17]. These simplified detector response curves were used in the diffusion analysis below.

3. DIFFUSION MODEL

This section describes a model for the diffusive loss of counter-passing MeV ions across the passing/trapped boundary and into our detector. Additional details concerning this model can be found in an extended version of the present paper [18].

Sections 3.1–3.5 describe the basic elements of the diffusive loss model *without* including the effect of the particle energy change during the slowing down process, while Section 3.6 describes this complicating but important effect. Applications of this model to experimental results are discussed in Section 4. Other possible loss processes are outside the scope of the present model, but they are discussed briefly in Section 5.2.

3.1. Diagram of first-orbit and diffusive loss regions

The experimental set-up illustrated in Fig. 1 can be clarified using the diagram shown in Fig. 4. For example, the orbits A–C of Fig. 1 are represented by the

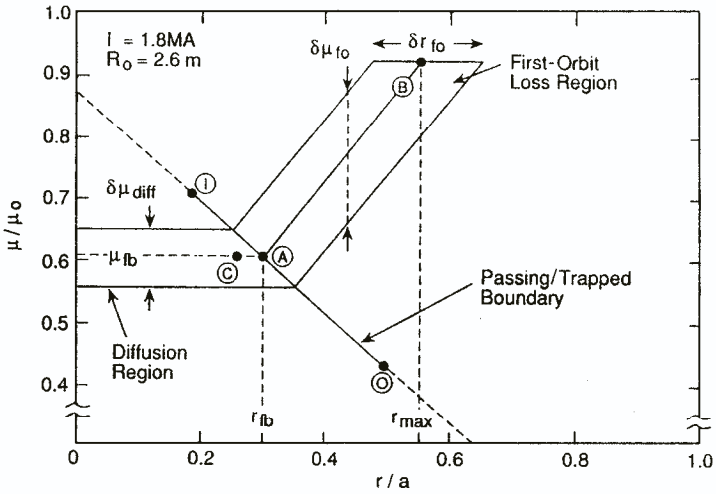

FIG. 4. Schematic diagram of all possible birth-energy guiding centre orbits for a 1.8 MA plasma in TFTR, showing the normalized ion magnetic moment μ/μ_0 versus the minor radius crossing point r/a of the outer midplane ion guiding centre. The first-orbit loss region is defined by the magnetic moment (i.e. pitch angle) of the fattest banana orbit, μ_{fb}, the maximum detectable μ, μ_{max} (at $\chi \approx 85°$) and the detector acceptance width in radius, δr_{fo}. The diffusive loss region is defined by the radial location of the fattest banana orbit r_{fb} and a fraction of δr_{fo} determined by the slope of the passing/trapped boundary line κ_{pt}. This particular diagram was drawn from many ORBIT code calculations (using a simplified current profile $j(r) \propto [1 - (r/a)^2]^3$). Note that the MeV ion source profile is heavily weighted towards r = 0.

points labelled A–C in Fig. 4. This particular diagram is drawn for the same typical 1.8 MA ($R_0 = 2.6$ m) TFTR plasma as used for Fig. 1.

This type of diagram represents (almost) all MeV ions of energy E by two parameters: the minor radius crossing point r/a of the outer midplane ion guiding centre (measured relative to the Shafranov shifted magnetic axis, choosing the smaller crossing point for trapped ions) and the ion's magnetic moment μ. The co-ordinate r/a is also a measure of the particle's toroidal canonical angular momentum (for a given magnetic geometry), which is conserved in axisymmetric systems but variable in the presence of turbulence (for example). μ is normalized to $\mu_0 = E/B_0$, where B_0 is the toroidal field at R_0. Note that the magnetic moment is normalized to an energy dependent μ to reflect the fact that for the high energy ions the classical slowing down process conserves μ/μ_0 (i.e. pitch angle scattering is small), so that during the slowing down process these MeV ions should remain at nearly the same vertical co-ordinate in this diagram.

Figure 1 was drawn for 1 MeV triton orbits in a typical 1.8 MA plasma. Since the other D–D fusion product (3 MeV proton) has an identical gyroradius and orbit diagram, in the following discussion these two D–D fusion products will be treated together as 'MeV ions' of birth energy E_0.

Note that this simplified 1-D spatial description assumes toroidal and poloidal symmetry in the MeV ion source profile, but incorporates the Shafranov shifted flux surfaces by defining r = 0 as the magnetic axis (the poloidal orbit average of the source profile is discussed in Section 3.4). Only the region r > 0 is considered here, which excludes a small class of co-passing unconfined orbits at small μ which cross the midplane only near the inner wall with a negligible ion population (see also Section 4.5). Note that this representation also does not show explicitly the inward shift of the counter-passing orbits with respect to the magnetic axis; thus, in this case the outer midplane crossing radius r is somewhat smaller than the half-diameter of the largest confined counter-passing orbit (see Section 3.4).

An important feature of Fig. 4 is the passing/trapped boundary line, which separates passing orbits (lower left) from trapped orbits (upper right). The line shown in Fig. 4 was drawn on the basis of many individual orbit calculations which varied the initial values of r

and μ for 1 MeV tritons (equivalent to 3 MeV protons). This line can be defined as

$$\mu/\mu_0 \approx [0.9 - \kappa_{pt}(r/a)] \quad (3)$$

where κ_{pt} is the slope of the passing/trapped boundary line. Theoretically, $\kappa_{pt} \approx (a/R_0)(1 + 2\Delta_c/r)$, where Δ_c is the shift of the centre of the marginally counter-passing orbit from the magnetic axis.

The fattest banana orbits on the passing/trapped boundary line at smaller r/a correspond to orbits which intersect the vessel nearer the inner midplane, and points on the passing/trapped boundary at larger minor radii intersect the vessel nearer the outer midplane. The points I and O in Fig. 4 represent the fattest banana orbits which hit the inner and outer midplanes, respectively.

The two enclosed regions in Fig. 4 represent the expected populations of first-orbit and diffusive loss to the detector location at the vessel bottom. A calculation of the number of MeV ions born within the first-orbit loss region is presented in Section 3.2 and a calculation of the maximum possible loss to the same detector via spatial diffusion at constant μ/μ_0 across the passing/trapped boundary is presented in Section 3.3.

Before proceeding with the analysis, we note that the radial loss across the passing/trapped boundary can, in general, be due to both a real space diffusion D (m^2/s) and a velocity space diffusion in pitch angle. Even though the classical pitch angle scattering rate of energetic ions is small, the rate of velocity space diffusion across the passing/trapped boundary (i.e. vertically in Fig. 4) may not be negligible compared to the effect of a very small spatial diffusion rate. In addition, the spatial diffusion rate may in general increase towards the passing/trapped boundary owing to an enhanced velocity space scattering effect. However, in the present paper we neglect the possible pitch angle scattering into the detector acceptance region and assume that D is constant in space within the region of confined counter-passing ions. A more complete treatment of these effects would only result in a reduction of the already small upper bound on the spatial diffusion rate D inferred from the data (see also Section 5.3).

3.2. First-orbit loss flux

The first-orbit loss is determined by the source strength within the first-orbit loss region shown in Fig. 4. The largest loss occurs near the fattest banana orbit, which has a magnetic moment μ_{fb} and a toroidal pitch angle χ_{fb}, where again we define the orbit's pitch angle χ at the detector with respect to the local toroidal field (i.e. $\chi = 0°$ corresponds to an ion directed along B_0 at the detector). Thus, for example, the fattest banana orbit has $\mu_{fb} = E_0 \sin^2[\chi_{fb} - \chi_b]/B_0$, where χ_b is the angle of the total magnetic field at the detector with respect to B_0. For the 1.8 MA case, $\chi_{fb} = 59° \pm 2°$ and $\chi_b \approx 6° \pm 2°$ (note that the detector radius of 2.59 m is very close to $R_0 = 2.6$ m).

The first-orbit acceptance range in μ of the detector is determined by its acceptance range in χ, which is $\chi \approx 45°$–$85°$ for the present detectors (which were rotated co-22.5° from the radial direction, to be centred near χ_{fb}). When the pitch angle at the detector is varied between $\chi_{fb} \approx 59°$ and $\chi_{max} \approx 85°$, the location of the resulting orbits in the diagram of Fig. 4 varies on a straight line from point A to point B, at r_{max} (and μ_{max}), i.e. roughly

$$\mu_{fo}/\mu_0 \approx 0.1 + \kappa_{fo}(r/a) \quad (4)$$

where $\kappa_{fo} \approx 1.3$ for the case in Fig. 4. Note that orbits with $\chi < \chi_{fb}$ are unconfined co-going orbits which have midplane crossings near the inner wall and so represent a negligible source population (see also Section 4.2).

The detector acceptance range in r is indicated schematically in Fig. 4 by the width δr_{fo} around orbit B. This δr_{fo} is determined by the range of radii over which ions of a given magnetic moment can enter the detector aperture (for clarity, the actual $\delta r_{fo} \approx 10^{-3}$ m is greatly exaggerated in Fig. 4). Note that δr_{fo} drops out in the final analysis, since it is a common factor in both the first-orbit loss and the diffusive loss (the same is true for the toroidal acceptance width, assuming toroidal symmetry of the source and loss).

Thus, the first-orbit loss flux Γ_{fo} to the detector is the integral of the local MeV ion source rate $S(r, \mu)$ over the first-orbit loss area of Fig. 4:

$$\Gamma_{fo} \propto \int S(r, \mu) r dr d\mu \quad (5)$$

where cylindrical geometry is taken into account in the radial integral. The source function can be separated into a radial part and an angular part using

$$S(r, \mu) = S(r)S(\mu) = S(r)(1 - \mu/\mu_0)^{-1/2} \quad (6)$$

where the μ-dependent factor has been evaluated for an isotropic fusion product source. Defining $\delta\mu_{fo}$ to be the acceptance range in μ for first-orbit loss, this can be rewritten:

$$\Gamma_{fo} \propto \delta\mu_{fo}\langle S(\mu)\rangle_{fo} \int_{r_{fb}}^{r_{max}} S(r) r dr \quad (7)$$

where the source integral is taken over the range of midplane radii for first-orbit loss. The average value of the μ-dependent source variation $\langle S(\mu)\rangle_{fo}$ is to be calculated from Eq. (6), and the range of detected μ at each r (from Fig. 4) is

$$\delta\mu_{fo}/\mu_0 \approx \kappa_{fo}\delta r_{fo}/R_0 \tag{8}$$

where we have used the slope of the first-orbit line from A to B (κ_{fo}). Note that, since first-orbit loss is very rapid (≈ 1 μs) Eq. (7) is valid on all time-scales of interest, including the steady state.

3.3. Maximum possible diffusive flux

Turning now to the diffusive loss, the first issue is the magnitude of the *possible* diffusive loss compared with the expected first-orbit loss. In this section the maximum possible diffusive loss is calculated in the limit $D \rightarrow \infty$, and the result is expressed in term of Ω, defined as the ratio of the maximum possible diffusive loss to first-orbit loss (for this detector).

We assume (for this section) that the MeV ions diffuse at constant μ/μ_0 and remain near their birth energy E_0, thus constraining the detectable ions to a horizontal band of width $\delta\mu_{diff}$ around μ_{fb}, as shown in Fig. 4. All ions born in this diffusion region can potentially cross the passing/trapped boundary within the region viewed by the detector, while all of the passing ions born outside this band diffuse across the passing/trapped boundary elsewhere and so cannot be detected within the region defined by δr_{fo}.

The height of the diffusion region in μ_{diff} is set by the distance along the passing/trapped boundary within which lost orbits can enter the detector. This in turn is set by the radial detector acceptance width δr_{fo} (which is approximately independent of μ) and by the slope of the passing/trapped boundary line κ_{pt}. From the geometry of the intersection of the detector acceptance width δr_{fo} with the passing/trapped boundary shown in Fig. 4, we obtain (after some algebra)

$$\delta\mu_{diff}/\delta\mu_{fo} \approx \kappa_{pt}/(\kappa_{fo} + \kappa_{pt}) \tag{9}$$

Thus the *maximum possible* diffusive flux to the detector, corresponding to an infinite radial diffusion coefficient for MeV ions, is proportional to the source weighted area of the diffusive region in Fig. 4 extending from r = 0 to r = r_{fb}:

$$\Gamma_{diff,\infty} \approx \delta\mu_{diff}\, S(\mu_{fb}) \int_0^{r_{fb}} S(r)\,r\,dr \tag{10}$$

An important parameter in the data analysis is the ratio of this maximum possible diffusive flux to the detector to the expected first-orbit loss to the same detector:

$$\Omega \equiv \Gamma_{diff,\infty}/\Gamma_{fo} \tag{11}$$

or

$$\Omega = (\delta\mu_{diff}/\delta\mu_{fo})(S(\mu_{fb})/\langle S(\mu_{fo})\rangle) \times \int_0^{r_{fb}} S(r)\,r\,dr \Big/ \int_{r_{fb}}^{r_{max}} S(r)\,r\,dr \tag{12}$$

Now, from Eq. (9) the ratio of the $\delta\mu$ widths is

$$\xi_\kappa = \delta\mu_{diff}/\delta\mu_{fo} \approx \kappa_{pt}/(\kappa_{fo} + \kappa_{pt}) \tag{13}$$

and, since $S(\mu)$ is a weakly varying function of μ in the range of interest, we can simplify the μ-weighting factor:

$$\xi_\mu \equiv S(\mu_{fb})/\langle S(\mu_{fo})\rangle \tag{14}$$

Typically, $\xi_\mu \approx 0.8$, as evaluated from Eq. (6) for Fig. 4. Thus, the final result for the $D \rightarrow \infty$ is

$$\Omega \approx \xi_\kappa \xi_\mu I(r_{fb}) \tag{15}$$

where the radial source integral is

$$I(r_{fb}) = \int_0^{r_{fb}} S(r)\,r\,dr \Big/ \int_{r_{fb}}^{r_{max}} S(r)\,r\,dr \tag{16}$$

i.e. (r_{fb}) is the integral of the number of ions born within the confined region inside r_{fb} divided by the number of ions born in the first-orbit loss region outside r_{fb}, as evaluated for a magnetic moment near that of the fattest banana orbit of this detector.

Note again that although the integrals in $I(r_{fb})$ are to be evaluated using the 1-D model source function S(r), this integral should ideally take into account the entire 2-D orbit averaged source for D–D fusion products crossing the outer midplane at r_{fb}. Note also that the $D \rightarrow \infty$ limit used here is consistent with the assumption of a negligible change in energy or μ for MeV ions during their diffusion; thus, Eq. (12) for Ω does not need any further correction for energy loss effects (see also Section 3.7).

The parameter Ω is crucial to the analysis of diffusive loss in this experiment, since, if $\Omega < 1$, the diffusive loss can *never* dominate the first-orbit loss. However, if $\Omega \gg 1$, then even a small diffusion coefficient could

cause enough loss to significantly change the character of the measured signals.

3.4. Evaluation of radial source integrals $I(r_{fb})$ and Ω

The ratio of maximum diffusive losses to first-orbit losses Ω in Eq. (12) depends crucially on the radial profile of the MeV ion source S(r), which is defined in the context of the 1-D cylindrical model of Sections 3.1–3.3 as the local MeV ion source rate measured along the outer midplane. Since the MeV ion orbits are not poloidally symmetric (see Fig. 1), the correct S(r) for a given r should be found by integrating the orbits passing through r (and μ) of the outer midplane over the actual 2-D source profile.

The radial source profile itself, $S_n(r)$, can be found from Abel inversions of multichannel neutron collimator measurements [19]. However, for the present paper the profiles from the SNAP transport code were used, partly because these could be read directly into the ORBIT code. These calculated source profiles included all neutron sources, i.e. beam–target, beam–beam and thermonuclear reactions, and agreed well with recent inversions of the actual measured profiles for some of these shots (see Appendix 4 of Ref. [18]). The SNAP source profiles can also be parametrized by a Gaussian with the full width at half-maximum (FWHM) centred at the major radius R_0:

$$S_n(R) = S_n(0) \exp(-[(R - R_0)/0.6\,\mathrm{FWHM}])^2 \qquad (17)$$

Typical experimental values for 1.8 MA plasmas were FWHM/a $\approx$ 0.55–0.60 (see Table II).

The source integral ratio $I(r_{fb})$ was numerically computed with the ORBIT code by integrating the source function over a large number of orbits within the first-orbit and diffusive loss regions of Fig. 4, using the SNAP neutron source and plasma current profiles in the ORBIT code. This takes into account the full poloidal asymmetry of the orbits (including non-fattest banana orbits such as B), the lingering near banana tips of orbits near the passing/trapped boundary, and finite gyroradius effects. Details of this calculation procedure are described in Appendix 2 of Ref. [18].

The result for a 1.8 MA shot (#55164) was $I(r_{fb}) \approx 6 \pm 2$. This result was then multiplied by the $\delta\mu$ weighting factor $\xi_\kappa \approx 0.4$, determined by Eq. (9) from the slopes of the passing/trapped and first-orbit loss lines from a figure such as Fig. 4 (with $\kappa_{pt} \approx 0.8$). No explicit correction for ξ_μ was made in this procedure, since this factor is implicit in the numerical orbit integrations for an assumed isotropic source.

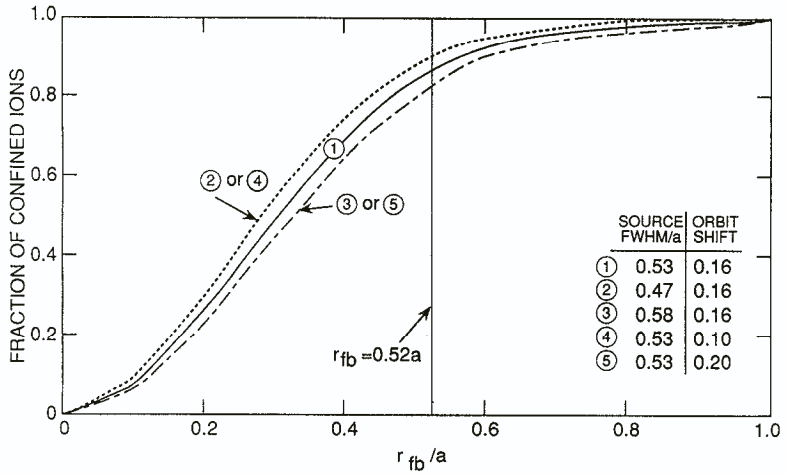

FIG. 5. Calculated fraction of MeV ions born within an orbit half-diameter r_{fb*}/a for various assumed source profiles and orbit shifts (with respect to the plasma minor axis). For example, given an orbit with minor radius $r_{fb*}/a = 0.52$ and an orbit shift of 0.16 (corresponding to the 1.8 MA case), the confined fraction is ≈ 0.87 for a Gaussian source profile width of FWHM/a = 0.53, and the corresponding first-orbit loss fraction is 0.13.

Therefore, the result of this analysis was $\Omega = \xi_\kappa I(r_{fb}) \approx 2.5 \pm 1$ for the 1.8 MA case, i.e. the maximum possible diffusive loss was about 2.5 times the expected first-orbit loss. Values of Ω calculated in the same way for other plasma currents are shown in Table II.

A simplified auxiliary model was used to understand the uncertainties in $I(r_{fb})$ which cause the relatively large uncertainties in Ω. Figure 5 shows the integral of the source profile between $r = 0$ and $r = r_{fb*}$, where r_{fb*} is the half-diameter of the largest passing orbit with μ_{fb}. At $r_{fb*}/a = 0.52$, corresponding to the 1.8 MA case, the confined population inside r_{fb*} is much larger than the first-orbit population and so the ratio of the two populations is quite sensitive to small variations in the first-orbit population caused by profile variations. For example, an uncertainty in the source FWHM of about 10% (for FWHM/a = 0.58–0.53) causes a variation in $I(r_{fb*})$ of about 25% (from $\approx$7.5 to 4.5), with similar effects due to uncertainties in the orbit parameters Δ_c and r_{fb}. Considering the plausible uncertainties in the source profile measurements and the orbit trajectory calculations (which depend on the plasma current profile), it is clear that estimates of Ω for cases similar to the 1.8 MA case used here are uncertain by approximately $\pm$30%.

3.5. Numerical solutions for finite D

Comparisons with experiment were made using a numerical solution of the cylindrical diffusion equation for the local number density of MeV ions n(r, t):

$$\partial n(r,t)/\partial t = D\{(1/r)\partial/\partial r[r\partial n(r,t)/\partial r]\} + S(r,t) - n(r,t)/\tau_{sE} \quad (18)$$

where $\Gamma_{diff} \propto Drdn/dr$ is the diffusive flux across the passing/trapped boundary, at which point $n(r_{fb}, t) = 0$. Although, for simplicity, D, τ_{sE} and the fattest banana radius r_{fb} were assumed to be constant in space and time, a realistic space–time dependence of the form $S(r, t) = S(r)S(t)$ was used to simulate the TFTR MeV ion (neutron) source. For comparisons with experiment the contribution to the expected signal due the first-orbit loss flux Γ_{fo} (proportional to the source rate) was added to the diffusive solutions found from Eq. (18). The first-orbit loss level was incorporated by scaling down the numerical result for $D \rightarrow \infty$ by a factor of $1/\Omega$.

A few sample solutions are shown in Fig. 6. For these cases the diffusion coefficient was varied between $D = 0$ and $D = 10$ m^2/s (effectively infinity) for fixed $\tau_{sE} = 0.6$ s, $\Omega = 2.5$ and $r_{fb*}/a = 0.52$ m for the 1.8 MA case. Here, τ_{sE} was chosen to be the central triton energy decay time in the 1.8 MA TFTR plasmas used for the experiment, where $T_e(0) = 5.5$ keV and $n_e(0) = 3.3 \times 10^{19}$ m^{-3} (the collisional energy e-folding decay time varied from 0.6 s at r = 0 to 0.45 s at r = a/2). For the solutions in Fig. 6, the source profile shape was chosen to be $S(r) \propto (1 - (r/a)^2)^8$, on the basis of fits to the neutron profile data, and the source time dependence S(t) was chosen to have an exponential rise time of 0.1 s, a duration of 1 s and an exponential

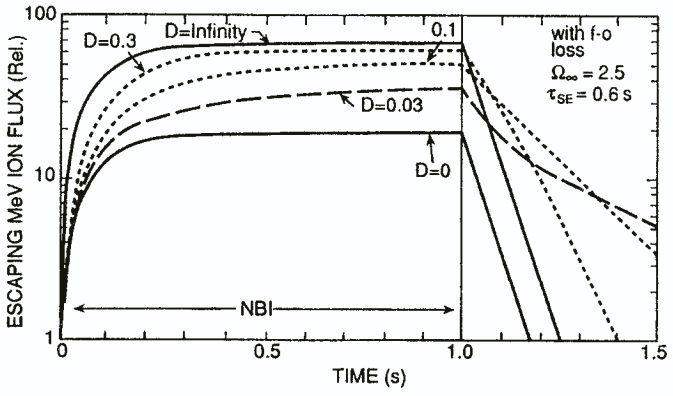

FIG. 6. Example of a calculation of the time dependent flux across the passing/trapped boundary (plus the first-orbit loss) as a function of the assumed MeV ion diffusion coefficient D. The assumed first-orbit loss is given by the D = 0 curve, which is proportional to the neutron source strength versus time. This case corresponds to tritons at 1.8 MA, where the assumed τ_{sE} is 0.6 s and the assumed Ω is 2.5.

decay time of 0.06 s, corresponding to the approximate time dependence of the global neutron rate in the 1.8 MA discharges.

Two qualitative features of the solutions in Fig. 6 are worth noting:

(1) About half of the maximum possible steady state diffusive flux occurs when $D \approx 0.1$ m^2/s, which is roughly consistent with the simple estimate $D \approx r_{fb}^2/4\tau_{sE}$ for significant diffusive loss of a peaked source in a cylinder (see Section 2.1).

(2) The results for the time period $t > 1$ s after the source is turned off suggest a sensitive means of identifying diffusion, since for $D = 0.01$–0.1 m^2/s the diffusive loss is significantly delayed with respect to the first-orbit loss. This result is analysed more fully in the next two sections. However, it is important to note that for $D \gg 0.3$ m^2/s the relative time dependence of the total loss is very similar to that of the first-orbit loss, since the loss time is much less than the slowing down time. In the limit $D \rightarrow \infty$, all ions are lost immediately, implying that the loss rate exactly follows the source, without any delayed loss.

3.6. Energy dependent numerical solutions for finite D

In the model used so far, all MeV ions above the detection threshold were lumped together into a single MeV ion density $n(r, t)$, and it was assumed that all ions had a characteristic slowing down time τ_{sE} between their birth energy and this detection threshold. This model would suffice if the detector system were equally sensitive to all detectable ions and if there were only one MeV ion species. However, the detector responds to both tritons and protons, and these responses are energy dependent, as shown in Fig. 3.

A kinetic equation for the energy distribution function $f(E)$ of ions subject to both classical slowing down and radial diffusion is

$$\partial f(E)/\partial t = (1/r)\partial/\partial r[rD\partial f(E)/\partial r] + C[f(E)] + S(r, t)\delta(E - E_0) \quad (19)$$

where $C[f(E)] = (E^{-1/2})(1/\tau_s)\partial/\partial E[E^{3/2} f(E)]$ is the collision operator, τ_s is the (1/e) energy decay time (assumed to be constant), and the ions are born at energy E_0. Assuming that the radial profile of the source function is $S(r) = kJ_0(x_1 r/a)$, i.e. a zero-order Bessel function with its first zero-crossing point at the passing/trapped boundary, a simple steady state solution was found to be

$$f_{ss}(E, r) = (k\tau_s/E_0)(E/E_0)^{\eta - 1} J_0(x_1 r/r_{fb}) \quad (20)$$

where $\eta \approx 5.6D\tau_{sE}/r_{fb}^2$ is the ratio of the slowing down time to the diffusive loss time. Thus, the energy spectrum of the confined ion population which diffuses across the passing/trapped boundary in steady state (proportional to $\partial f(E, r)/\partial r$ at r_{fb}) has the approximate form

$$f_{ss}(E)dE \propto (E/E_0)^{-1}(E/E_0)^{\eta} dE \quad (21)$$

In the limit of small diffusion, $\eta \ll 1$, the energy spectrum approaches the well known E^{-1} dependence (note the differential element dE, which contains an extra $E^{-1/2}$ factor compared with the v-distribution), while, in the limit of $D \rightarrow \infty$, the second term becomes dominant and the spectrum approaches a δ-function at E_0, as expected. For intermediate D, the low energy portion of the energy spectrum is attenuated by the diffusive effect, since these ions most likely have already diffused out of the system.

Note that for a typical experimental situation the energy spectrum effectively reaches a steady state after about $\tau_s \approx \tau_{sE}$ ($\approx$ 0.2–0.6 s), well before the end of a typical NBI pulse of 1 s duration. Note also that the results of the numerical calculations for the total escaping flux are not very sensitive to the precise form of the assumed energy spectrum.

For the time period after NBI when the source is turned off, each confined MeV ion loses energy at approximately the same e-folding rate (as long as E is above the critical energy were ion drag becomes significant, which is about 250 keV for tritons and 100 keV for protons [8]). Thus, the maximum energy at a time δt after then end of NBI is reduced from its birth energy E_0 by δE, where

$$\delta E = E_0(1 - \exp(-\delta t/\tau_s)) \quad (22)$$

The approximate solution used in the numerical calculations assumed that all components of the energy distribution function lose energy at a rate $\delta E/\delta t$ after NBI. Note that also this solution does not include in the spectrum those ions born during the source decay period after NBI.

To calculate the diffusive MeV ion loss corresponding to lower energy particles, a variable-energy form of the μ versus r presentation of Fig. 4 is needed. Figure 7 shows an example of the location of the passing/trapped boundary line for a partially thermalized 0.5 MeV triton, together with the first-orbit loss line and the passing/trapped boundary for 1.0 MeV tritons (as in Fig. 4). Note that the normalized vertical axis is still

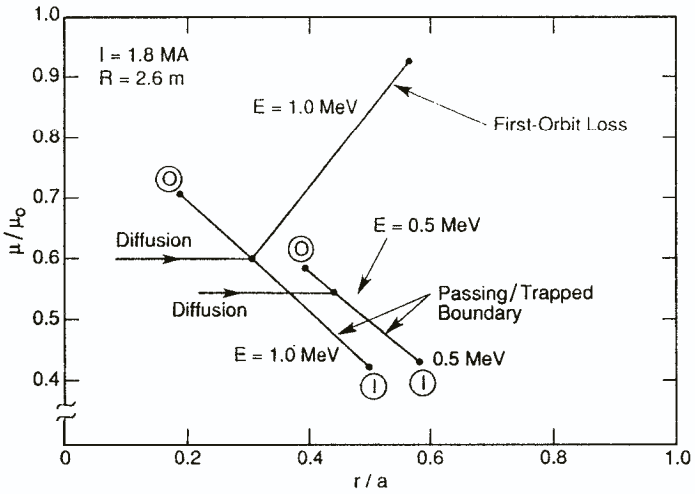

FIG. 7. Diagram structured like Fig. 4, showing μ/μ_0 versus r/a, but including the passing/trapped boundary for partially thermalized 0.5 MeV tritons. The passing/trapped boundary line moves to slightly higher r/a for lower energy ions, but diffusive loss to the bottom detector should still occur at nearly the same μ (i.e. the pitch angle).

$\mu/\mu_0 = \sin^2\chi$, which depends only on the orbit pitch angle (since μ_0 itself is energy dependent). Therefore, since particles remain at nearly the same μ/E and χ during classical thermalization (for $E > E_c$), they still diffuse approximately horizontally in r/a during thermalization. Note that pitch angle scattering can cause μ/μ_0 to change slightly as the diffusing ions thermalize, but we can safely assume that such scatterings into and out of the diffusion region compensate each other, since $\delta\mu_{diff}/\mu_0 \ll 1$.

The main energy dependent feature brought out by Fig. 7 is that, because of the decreased banana width at lower energy, the midplane minor radius of the fattest banana orbit r_{fb} increases as the energy of the ion decreases. This effect is *not* taken into account in the present model, which leads to a slight overestimate of the diffusive flux for a given D and thus a slight underestimate of the inferred D for a given experimental result. Note also from Fig. 7 that, although r_{fb} also slightly changes with energy, there are still approximately the same number of ions which diffuse to the new passing/trapped boundary, although these are not at the same magnetic moment as those which would have diffused there at constant energy.

For comparison with experiment, the energy independent diffusion code analysis based on Eq. (18) was first done separately for tritons and protons (as in Fig. 6), taking into account their different slowing down rates ($\tau_s \propto M/Z^2$). For the steady state case, the n(r, t) of MeV ion flux from Eq. (18) was distributed with the energy spectrum from Eq. (21), and the resulting spectrum was weighted according to the scintillator response for that ion using Fig. 3. The results for tritons and protons were then added together, weighted appropriately.

This energy spectrum correction of the expected diffusive loss signal is fairly large for tritons with a small D. For example, in the limit where D approaches zero, the scintillator response to a triton slowing down spectrum proportional to E^{-1} between E_0 and E_0/e is $\approx 20\%$ that for the same number of tritons at the birth energy E_0. However, the correction is smaller for protons, which cause a more constant scintillator response as a function of energy. The net result is that for moderate D the triton and proton scintillator responses to diffusive loss are usually comparable, since the smaller scintillator response for tritons is balanced by the larger confined triton population.

For the analysis of the time dependence after NBI, the same procedure was followed, except that the energy spectrum for each particle was changed according to Eq. (22). Thus, the proton contribution to the signal falls to zero after $t \approx \tau_{sE} = 0.2$ s, and the triton contribution falls to zero at $t \approx \tau_{sE} = 0.6$ s (for the 1.8 MA case). This attenuates the calculated flux after NBI for medium-D cases (such as for $D \approx 0.01$–$0.1\ m^2/s$

in Fig. 6), since the solutions without this energy correction fall with approximate e-folding times of τ_{sE} (see Section 4.8).

4. EXPERIMENTAL RESULTS

Four different measurements of the escaping MeV ion flux to the bottom of TFTR are now examined for diffusive effects, namely, the dependences on (a) plasma current, (b) pitch angle, (c) energy (gyroradius) and (d) time. For the sake of clarity, in Sections 4.1–4.4 the experimental results are compared with the first-orbit model without diffusion and in Sections 4.5–4.8 the same results are compared with the diffusive loss model.

Almost all of the data presented here were obtained from a 1 day experimental run on TFTR in 1990, during which the plasma current was varied in 0.4 MA steps from 0.6 to 1.8 MA, while keeping the plasma position fixed at $R_0 = 2.6$, the plasma minor radius fixed at $a = 0.95$ m, the toroidal field fixed at $B_0 = 3.73$ T on axis and the neutral beam pulse duration fixed at 3–4 s. This experiment was designed to minimize the effects of large scale MHD activity by operating at relatively low power, far from the usual beta limits of TFTR, but with enough neutral beam heating (5–12 MW) to produce an easily measurable MeV ion flux (corresponding to $(0.5–5) \times 10^{15}$ neutrons/s). Some additional data at 2.0 MA were obtained from a separate run with $R = 2.6$ m, but with $B_0 = 4.8$ T on axis, and somewhat more beam power. Although this dataset is relatively small, with only three to four discharges at each current, these results are quite reproducible and similar to the results obtained in 1988 [6]. A summary of the discharge parameters is given in Table I and corresponding model parameters are presented in Table II.

TABLE I. EXPERIMENTAL DISCHARGES

Shot No.	I (MA)	P_b (MW)	S_n (10^{15} s^{-1})
55170	0.6	4.6	0.61
55171	0.6	4.6	0.58
55172	0.6	4.6	0.57
55173	1.0	4.6	1.1
55176	1.0	4.6	1.1
55178	1.0	4.6	1.2
55179	1.4	12	5.3
55180	1.4	9.5	3.8
55181	1.4	9.5	3.7
55160	1.8	12	4.0
55161	1.8	12	4.9
55162	1.8	12	4.9
55182	1.8	16	9.2
54296	2.0	11	3.9
54308	2.0	13	6.0
54314	2.0	23	16

TABLE II. MODEL PARAMETERS[a]

I (MA)	r_{fb*}/a	Δ_c/a	$\tau_{sE}(0)$	FWHM/a	ϵ_{fo}	Ω
0.6	—	—	—	0.57	1.0	0
1.0	0.25	0.2	1.0	0.40	0.65	0.4
1.4	0.37	0.2	0.5	0.57	0.46	0.8
1.8	0.52	0.16	0.6	0.57	0.24	2.5
2.0	0.51	0.2	0.8	0.48	0.22	3.0

[a] r_{fb*}/a — interior radius of fattest banana (one-half of ± midplane crossings)
Δ_c/a — shift of interior leg of fb from the magnetic axis
$\tau_{sE}(0)$ — energy decay time to detector threshold
FWHM/a — full width at half-maximum of neutron source profile
ϵ_{fo} — relative first-orbit loss (summed over pitch angles of 45–85°)
Ω — ratio of maximum possible diffusive loss to first-orbit loss.

4.1. Plasma current dependence versus first-orbit model

The most important characteristic of first-orbit loss is that it decreases with increasing plasma current owing to the decreased banana width. Diffuse effects tend to increase the expected flux at the higher currents when the first-orbit loss becomes small.

Figure 8 is a set of contour plots showing, for various plasma currents, the light emission pattern from the 2-D scintillator detector at the bottom of TFTR, integrated over the approximately 'steady state' discharge time 3.5–4.0 s. The images for all currents in the range 0.6–2.0 MA show a single localized MeV ion impact region which moves in response to both plasma current and toroidal field. These images are interpreted using a map (also shown in Fig. 8) of the calculated co-ordinate

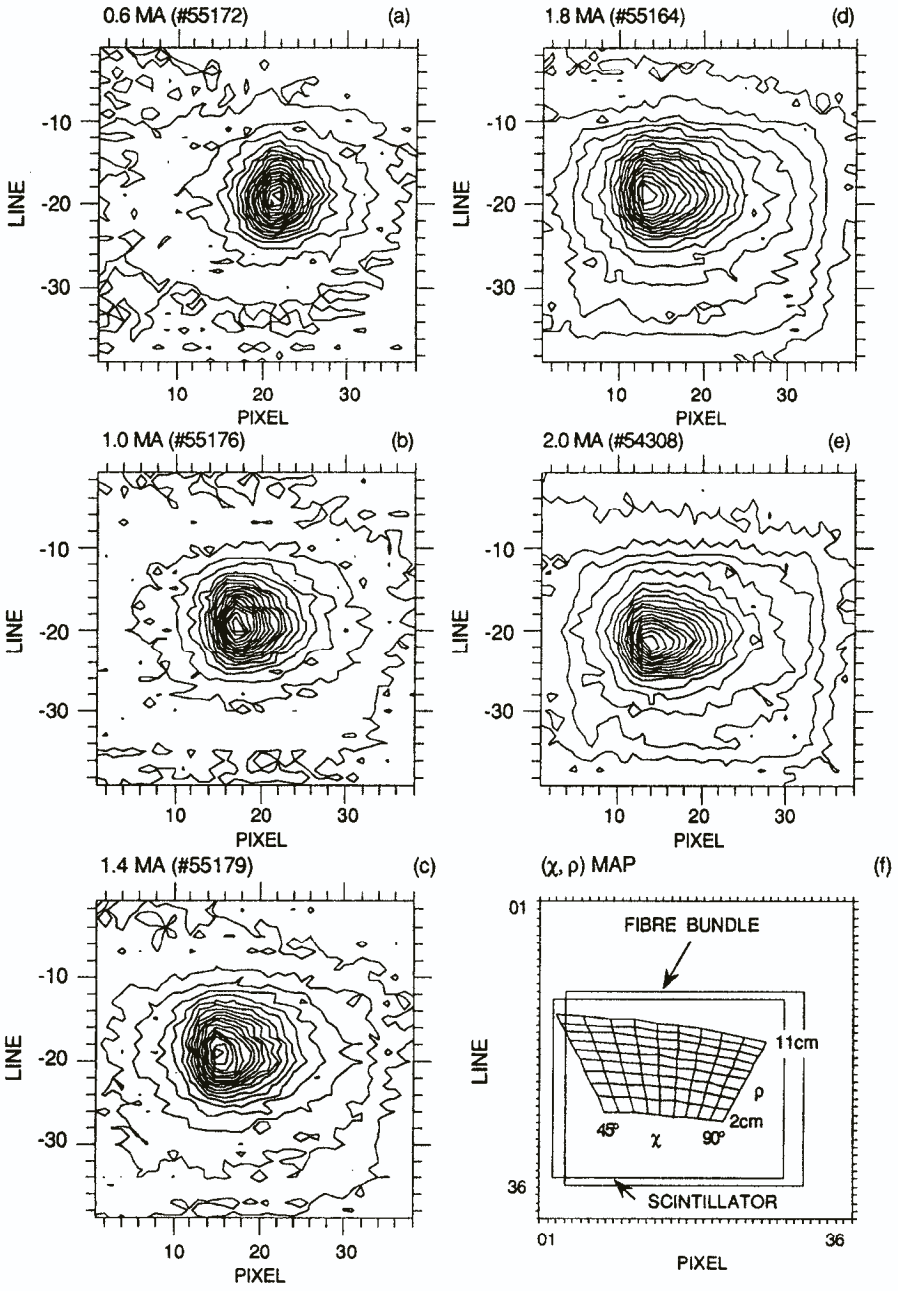

FIG. 8. Experimental contour plots showing the light emission pattern from the scintillator for various plasma currents, as viewed by the video camera. The line versus pixel format of the digitized images is interpreted using the map at the lower right, which shows centroids of calculated impact positions for various ion gyroradii ρ and pitch angles χ.

system of the scintillator in terms of gyroradius ρ and pitch angle χ, defined with respect to B_0 at the detector (i.e. $\chi = 60°$ corresponds to ions entering the detector at an angle of 60° to the co-B_0 direction). This map was made from a detector simulation code [6] which calculates the impact positions of a large number of orbits passing through the finite sized apertures and the 3 μm aluminium foil behind the slit, which is assumed here to reduce the ion energy by a factor of 0.8 (representing an average of the attenuation factors for 1.0 MeV tritons and 3.0 MeV protons of ≈ 0.65 and ≈ 0.95, respectively). Only the centroids of the impact 'footprint' for given ρ and χ are shown in Fig. 8 over the ranges $\rho = 0.02$–0.11 m and $\chi = 45$–$90°$ (note that the lines $\rho < 4$ cm should have an increased averaged foil attenuation factor, which is not taken into account here).

The contour plots of Fig. 8 were made using raw data, without normalization for the varying neutron source strengths and without correction for the nearly uniform background due to neutron/gamma lighting of the fibre bundle (or possibly the scintillator itself). However, this background was corrected for in all the following data by subtracting out the signal levels observed inside a corner region of the scintillator that was not hit by the MeV ions. This background was about 20% of the peak signal level at 1.8 MA, and less for lower plasma currents.

Figure 9 is a plot of the *total* observed MeV ion flux (within $\chi = 45$–$90°$ and $\rho = 0.02$–0.11 m) versus the plasma current for the whole set of discharges used for this experiment. For each shot these fluxes are averaged over 3.5–4.0 s and normalized by the averaged neutron rate during this period. The data show a clear reduction of this normalized flux by a factor of about five with increasing plasma current in the range 0.6–2.0 MA. The shot-to-shot variability at a given current (shown as an error bar) is within about $\pm 10\%$, which is typical for these experiments [6].

Also shown in Fig. 9 is the prediction of the first-orbit loss model for the relative loss versus the plasma current, also integrated over $\chi = 45$–$85°$. These total first-orbit losses were obtained from ORBIT code calculations using the SNAP derived plasma current and neutron source profiles for shots in this run (except for the 0.6 MA case, see below). The shape of the curve for the first-orbit model agreed well with the data. Note that the data were normalized to the model curve at 0.6 MA, which is the point at which the entire signal should be due to first-orbit loss only (see below). Note that the recent absolute calibration [17] had an uncertainty which was too large to be useful for normalization here (the experimental signals agreed with the calculated loss within an uncertainty of two to three).

At 1.8 MA, the points calculated with ORBIT are uncertain by up to $\pm 50\%$ owing to uncertainties in the plasma current and the plasma source profiles (see Appendix 4 of Ref. [18]). However, at 0.6 MA, the uncertainties in the model are only about $\pm 10\%$, since for all reasonable profile choices the detected orbits pass directly through the high source rate region at the plasma centre. The model value for 0.6 MA shown in Fig. 9 was derived from an assumed current profile shape of parabolic to the fourth power and a Shafranov shift of 0.24a (based on the electron temperature profile), and from a Gaussian approximation to the neutron source profile shape with FWHM/a = 0.55 measured with the multichannel collimator.

The data and the first-orbit model curve of Fig. 9 agree within the combined uncertainties of both. Therefore, the measured plasma current dependence of the MeV ion loss agrees well with the simple first-orbit model without diffusion, i.e. with D = 0. The effect of a hypothetical MeV ion diffusion on the expected plasma current dependence is discussed in Section 4.5.

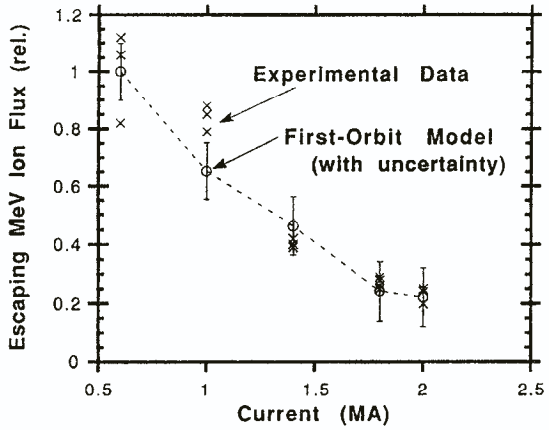

FIG. 9. Comparison between the total escaping MeV ion light flux, averaged over the steady state time 3.5–4.0 s (×), and the predicted first-orbit loss for various plasma currents (○). The measured points are obtained by integrating the MeV ion signals over the whole grid region $\rho = 0.02$–0.11 m and $\chi = 45$–$90°$ (see Fig. 8), and normalizing to the average neutron rate during this time (one × for each shot). The first-orbit model points are obtained by integrating the ORBIT code calculations over the same range in pitch angle. The model curve is normalized to the average of the data at 0.6 MA.

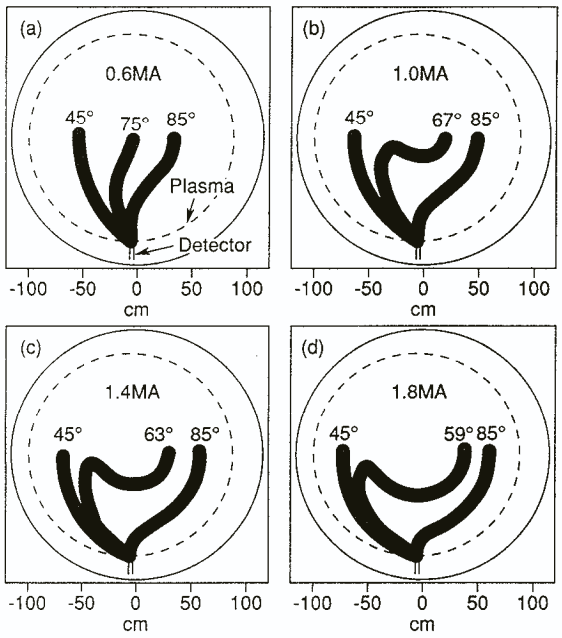

FIG. 10. Calculated orbit trajectories (at birth energy) observable from the bottom detector for several plasma currents. The pitch angles shown correspond to the detection limits (45–85°) and the particular pitch angle which most closely approaches the plasma centre. At 0.6 MA the orbits all move nearly vertically, while at 1.0–1.8 MA the orbits passing closest to the plasma centre have the 'fattest banana' shape.

4.2. Pitch angle distribution versus first-orbit model

The pitch angle dependence expected for first-orbit loss at the bottom detector was determined from many individual ORBIT calculations such as those shown in Fig. 10. For each plasma current, the orbit with the largest calculated flux (passing nearest the high source rate plasma centre) is shown, together with the first-orbit loss orbits for $\chi = 45°$ and $\chi = 85°$ (the detection limits).

For all currents above 1 MA, the orbits passing nearest the plasma centre have a characteristic 'fattest banana' shape, with a unique pitch angle χ_{fb} determined by the birth energy and the detector radius R_{det}. At 0.6 MA, there is no 'fattest banana', since the orbit nearest the centre moves nearly vertically downward. Note that χ_{fb} itself varies with current from $\approx 67°$ at 1.0 MA to 59° at 1.8 MA. This agrees with simple estimates, since in the limit of high current the fattest banana orbit reaching a detector at $R_{det} \approx R_0$ has $\sin \chi_{fb} \approx [1 - a/R_0]^{1/2} \approx 55°$, while for low currents the orbits passing nearest the centre reach the detector with a pitch angle $\chi_{fb} \approx 90°$, since these orbits move nearly vertically down to the detector.

The measured pitch angle distributions corresponding to the images of Fig. 8 are shown in Fig. 11 (integrated over the gyroradius range 0.02–0.11 m and over 3.5–4.0 s). Also shown are predictions from the first-orbit loss code, which were normalized to the measured peak height. The locations of the peaks and the shapes of the experimental pitch angle distributions agree well with first-orbit model predictions over the whole current range 0.6–2.0 MA.

Note that no adjusted parameters were used in this comparison, except for the vertical normalization. The model curves were taken directly from the ORBIT code outputs and smoothed by the geometrical pitch angle resolution of the detector ($\approx 3°$ FWHM) and the measured optical resolution ($\approx 9°$ FWHM). In the ORBIT code, SNAP generated plasma current profiles and D–D reaction rate profiles for these shots (including the Shafranov shift) were used, except for the 0.6 MA case (see Section 4.1). The experimental pitch angle scale was determined by an in situ optical alignment, with an alignment uncertainty of up to $\pm 3°$ (not shown).

The effect of diffusive loss would be to add a contribution to the detector signal just at the passing/trapped boundary, i.e. near the peak of the calculated first-orbit distributions. The resulting pitch angle distributions for various D values are described in Section 4.6.

4.3. Gyroradius dependence versus first-orbit model

If the observed loss were only first-orbit loss, the gyroradius should always be set by the birth energy, which implies $\rho = 0.068$ m for $B_0 = 3.7$ T as used for the cases with $I \leq 1.8$ MA (note that in this case ρ is defined as the gyroradius at $\chi = 90°$ at the detector radius $R_{det} \approx R_0$, which is the same for 3 MeV protons and 1 MeV tritons). The presence of MeV ion diffusion would inevitably lead to loss of lower energy (smaller gyroradius) ions.

Figure 12 shows typical gyroradius distributions for various plasma currents, all taken from the pitch angle averaged (45°–90°) distribution in Fig. 8 (averaged over 3.5–4.0 s). For all cases, the peak of the observed distribution is very near the expected location of the first-orbit loss, at least within the alignment uncertainty of about ± 0.01 m (not shown). For the 2.0 MA case at the higher value of $B_T = 4.8$ T, the gyroradius distribution shifts to near ≈ 0.05 m, as expected.

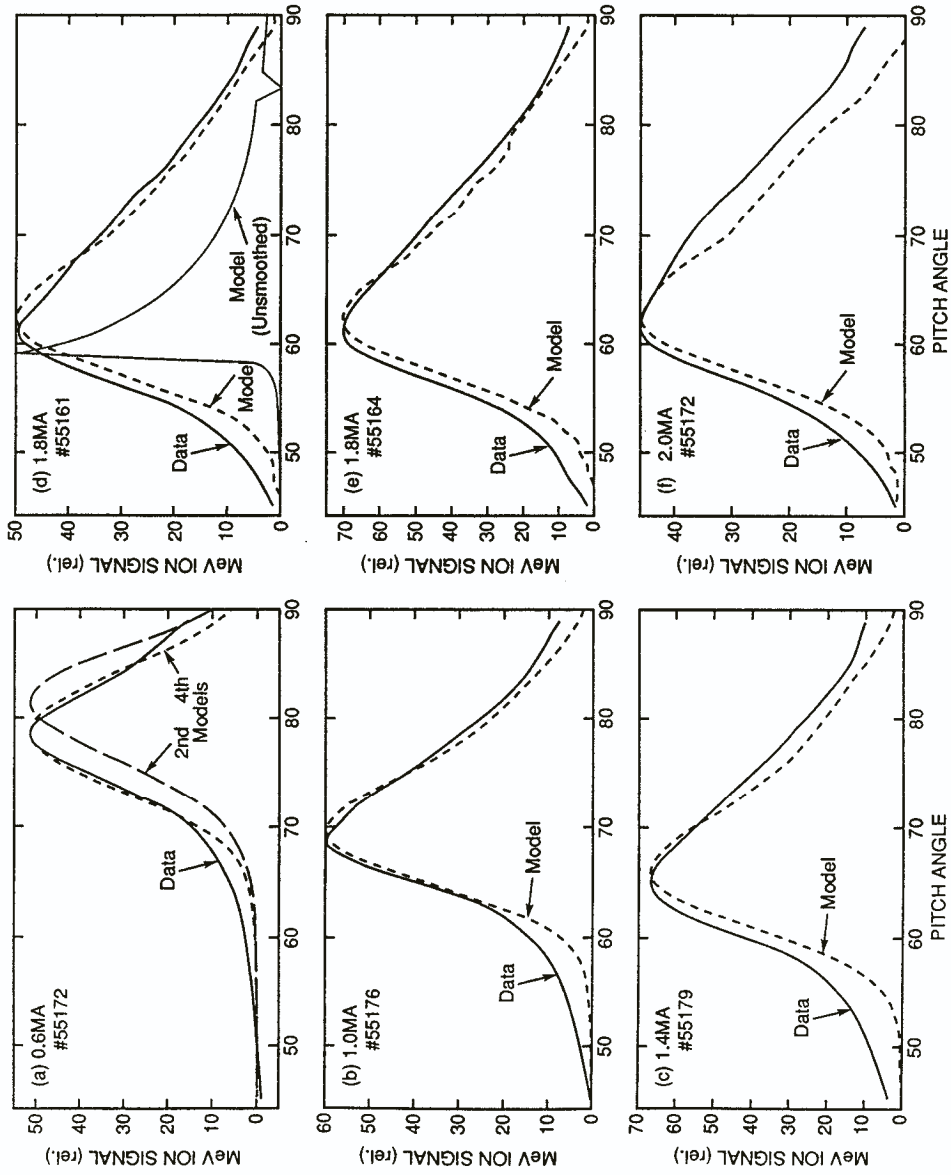

FIG. 11. Comparison between the measured and calculated pitch angle distributions for various plasma currents. The measured distributions are averaged over the grid in the range $\rho = 0.02$–0.11 m and over 3.5–4.0 s. The first-orbit loss distributions are taken from the ORBIT code calculations and smoothed according to the known instrumental broadening effects (an unsmoothed distribution is also shown for discharge No. 55161).

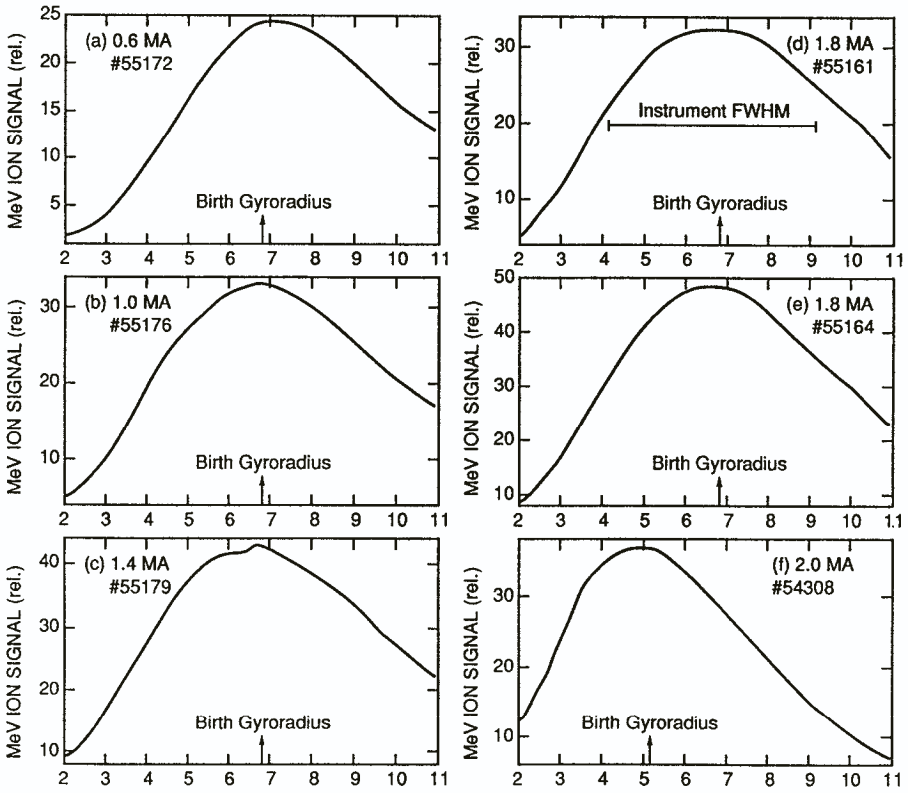

FIG. 12. Measured gyroradius distributions for various plasma currents and the expected gyroradius for first-orbit loss. The measured distributions are averaged over pitch angle (45–90°) and over 3.5–4.0 s. The widths of these distributions are due mainly to the instrumental broadening (shown for discharge No. 55161). Note the shift of both the measured and the predicted gyroradius for the high toroidal field case (No. 54308).

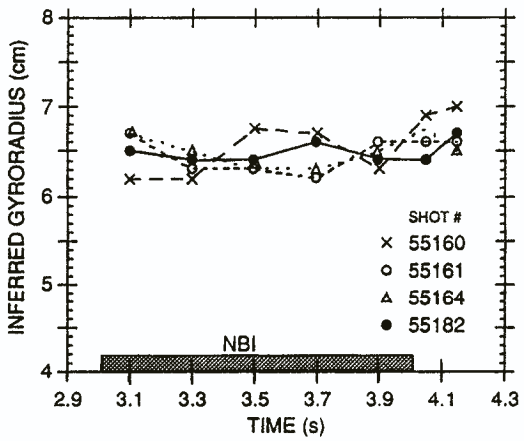

FIG. 13. Measured peak of the gyroradius distribution versus time for the four discharges at 1.8 MA. The peak location remains approximately constant near the expected first-orbit loss radius of ρ = 0.068 m (there is a systematic uncertainty of about ±0.01 m in these measurements).

The large widths of these distributions are set by the relatively poor gyroradius resolution of this detector, as determined by the detector simulation code [6]. This instrumental width, when folded in with the optical resolution (equivalent to about ±0.016 m), is roughly consistent with the observed widths, as shown by the FWHM bar in Fig. 12(d). This poor gyroradius distribution prohibits any serious attempt to unfold possible energy spectra, although the relative location of the gyroradius peak can provide some information about the average ion energy.

The location of the peak in the gyroradius distribution is plotted versus time in Fig. 13 for the four 1.8 MA discharges used in this experiment. To within the accuracy of these measurements, the peak gyroradius (as well as the peak pitch angle) remains constant in time during and after NBI. This constancy can be used to limit the diffusive effects, as discussed in Section 4.7.

4.4. Time dependence versus first-orbit model

Perhaps the simplest sign of diffusive loss would be the expected time delay between changes in the source (neutron) rate and the measured escaping flux. After the source is turned off, the diffusive loss can be delayed by as much as $\tau_{diff} \approx r_{fb}^2/D$ or $\approx \tau_{sE}$ (whichever is shorter), while the first-orbit loss should instantaneously follow changes in the source rate (integrated along the loss orbit).

Figure 14 shows the time dependence of the total escaping MeV ion flux to the detector versus the global neutron rate for typical 0.6 MA and 1.8 MA discharges. The relative time dependence of the global neutron rate and the MeV ion loss are similar, so that the lost MeV signal is nearly proportional to the MeV ion source rate, as expected for first-orbit loss. This result has been consistently observed in discharges without large coherent MHD activity [6].

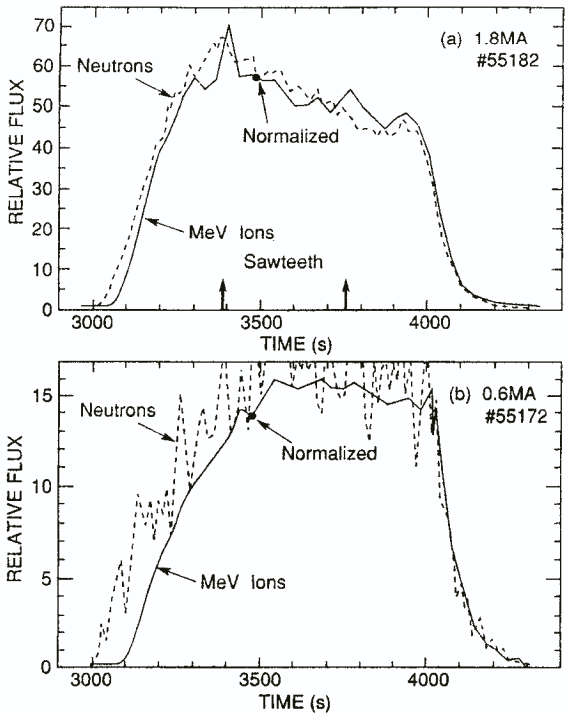

FIG. 14. Measured time dependence of the total MeV ions loss (integrated over χ = 45–90° and ρ = 0.02–0.11 m) versus the measured neutron rate (i.e. global MeV ion source rate) for 0.6 MA and 1.8 MA discharges. These two signals have very similar time dependences, particularly just after the end of NBI. The two signals are normalized to each other at 3.5 s. Sawtooth crashes for this shot are indicated by two arrows in (a).

In Fig. 15, the time dependence of the MeV ion loss for the 1.8 MA case is shown for various subregions of (ρ, χ) and compared with the global neutron rate. The shape of the MeV ion flux versus time is nearly the same at the largest (ρ = 0.09–0.11 m) and the smallest (ρ = 0.02–0.04 m) ends of the gyroradius distribution (at χ = 55–65°), and at the smallest (55–65°) and the largest (75–85°) ends of the pitch angle distribution (at ρ = 0.04–0.09 m). Thus, there is no evidence for delayed diffusive loss, even after NBI when the diffusive loss should be most apparent.

This absence of delayed MeV ion loss after NBI holds true for a wide variety of TFTR discharges. For example, Fig. 16 shows this similarity for a larger set of 1.6 MA discharges for two other run days, as measured using a video camera. This equivalence of the decay time of the MeV ion loss and the neutron rate after NBI was also seen with better time resolution when a phototube monitor of the MeV ion signal was used [6, 20].

However, in Fig. 14 there is an apparent delay in the start of the MeV ion loss (also observed in other studies [6, 20]) with respect to the start of the neutron emission, for example by up to 100 ms (at 0.6 MA). This is not understood in detail, although the most likely cause is a systematic variation in the D–D source or the plasma current profile during this early time period, such that the MeV ion loss fraction is reduced temporarily, for example owing to an unusually peaked source profile.

Thus, the observed time dependences are, at least qualitatively, consistent with the first-orbit model predictions. The expected effects of diffusion on the time dependence of the MeV ion loss rate after NBI is discussed in Section 4.8.

4.5. Effects of diffusion on the plasma current dependence

The simplest and ultimately the most important effect of MeV ion diffusion would be an increase of the total escaping MeV ion flux above the level expected for first-orbit loss. This effect should be clearest at high plasma currents when the first-orbit loss is relatively small.

The theoretical analysis of the possible effects of diffusion on the experimental results is described in Section 3. The main parameter in that analysis is Ω, the ratio of the maximum possible diffusive flux (in the limit $D \rightarrow \infty$ in steady state) to the expected first-orbit loss flux, calculated with respect to a particular detector location, plasma current, and current and neutron source profiles. The result for the 1.8 MA

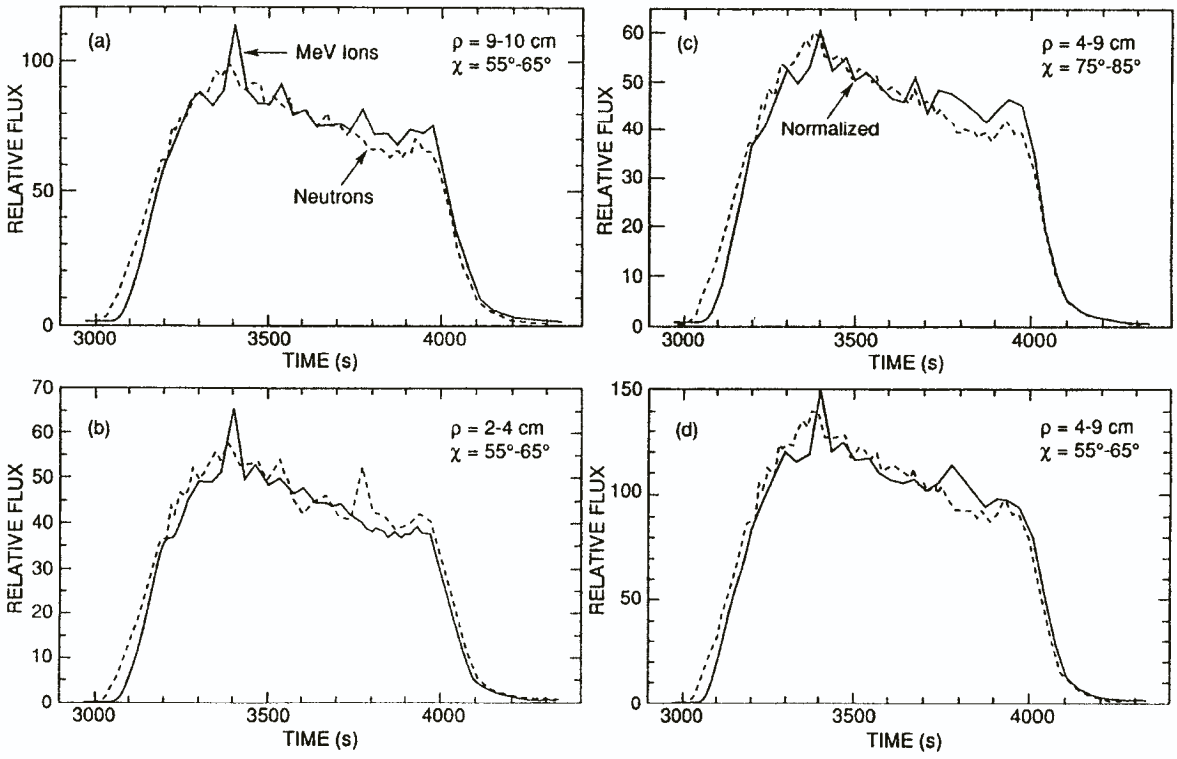

FIG. 15. Measured time dependence of the MeV ion loss within certain (ρ, χ) regions for the 1.8 MA discharge shown in Fig. 14. The time dependence is very similar within the regions ρ = 0.02–0.04 m and ρ = 0.09–0.11 m at χ = 55–65°, and within ρ = 0.04–0.09 m at χ = 55–65° and χ = 75–85°. The same global neutron rate versus time is used for all cases.

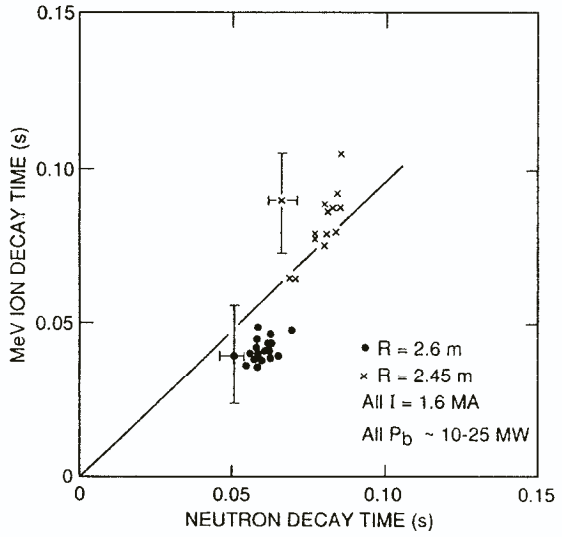

FIG. 16. Measured MeV ion decay time just after NBI versus neutron decay time for two sets of 1.6 MA discharges. These times were measured from the end of NBI to the time at which the respective signal decayed to (1/e) of its value at the end of NBI.

discharges of this dataset is $\Omega = 2.5 \pm 1$ (see end of Section 3.4).

The maximum possible diffusive loss for other currents was determined in the same way. For plasma currents of 1.0 MA and 1.4 MA, the calculated values of Ω were lower than those for 1.8 MA, i.e. $\Omega = 0.4$ and 0.8, respectively. This is due mainly to the smaller inner radius of the fattest banana orbits, as can be seen in the ORBIT pictures of Fig. 10. This effect can also be seen in Fig. 17, which shows the full r/a versus μ/μ_0 plots for various currents as determined from the ORBIT code, including both outer and inner midplane crossing regions in μ–r space. Note in particular that at 0.6 MA there is no fattest banana orbit and thus no confined counter-passing orbits are available for diffusion into this detector, i.e. $\Omega = 0$.

The plots of Fig. 17 also show another factor entering into the Ω calculation, namely the increased slope of the first-orbit loss line κ_{fo} with increased plasma current (as expected from the varying size of the banana width, see below Eq. (3)). Because of this increased slope, the relative height in μ of the first-orbit loss region,

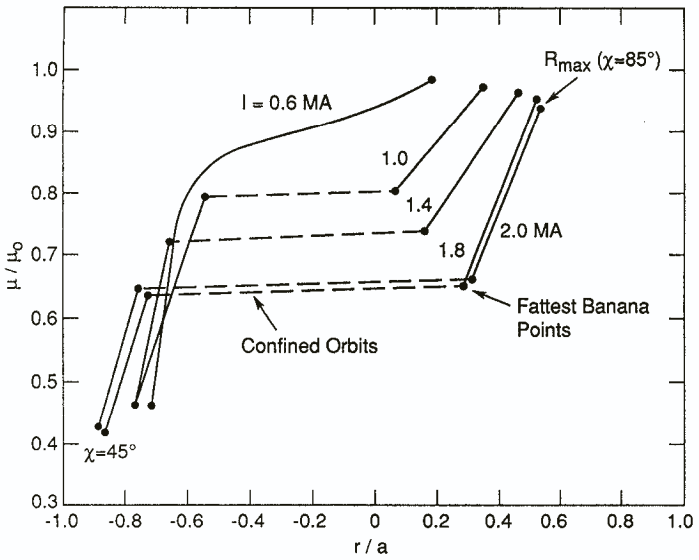

FIG. 17. Diagram similar to that presented in Fig. 4, but showing the first-orbit loss lines for the bottom detector (for χ = 45–85°), for various plasma currents. For 0.6 MA, the orbits lost to the detector cross the midplane everywhere between r/a = –0.7 and 0.2, while for the higher currents there is an increasingly large region of confined passing orbits (inside the fattest banana). The slopes of the first-orbit lines and the passing/trapped boundary lines vary with plasma current as shown.

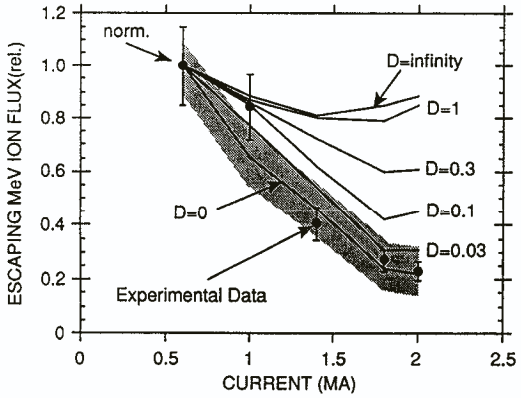

FIG. 18. Measured escaping MeV ion flux versus plasma current (from Fig. 9) compared with model curves calculated using various assumed values of D. The uncertainty in the D = 0 theoretical curve is indicated by the shaded area (also taken from Fig. 9). The data are consistent with D ≤ 0.03 m^2/s.

$\delta\mu_{fo}$, decreases somewhat at these lower currents, which increases the ξ_κ weighting factor for the lower plasma currents (as $\kappa_{fo} \rightarrow 0$, $\xi_\kappa \rightarrow 1$ from Eq. (9)). The resulting model parameters for varying currents are summarized in Table II; note again that the Ω estimates are uncertain by approximately ±30–50%.

These Ω values were used to plot the expected MeV ion signal versus the current for D → ∞. Figure 18 shows that there is a substantial difference between the shape of the D → ∞ model curve and that of the first-orbit model curve; for D → ∞, the expected flux decreases by only ≈20% between 0.6 and 18 MA, whereas the first-orbit loss decreases by a factor of nearly five.

At first sight, it may be surprising that the D → ∞ curve varies at all with current, since all the previously confined particles should be lost. However, Fig. 17 shows that for a given detector the location of the observable loss region varies in μ/μ_0 and r/a as the current varies (as does the height of the first-orbit integration region $\delta\mu_{fo}$), and therefore the maximum possible loss observable by a detector also varies somewhat with plasma current.

A comparison of the experimental results from Fig. 9 with the numerical solutions for finite D is also shown in Fig. 18. At face value, this comparison implies an upper limit for the MeV ion diffusion coefficient of D ≈ 0.03 m^2/s for the data points at 1.4, 1.8 and 2.0 MA (the uncertainties at 1.0 MA are too large for estimating D).

The uncertainties in the first-orbit loss for D = 0 (from Fig. 9) are shown in Fig. 18, but the uncertainties

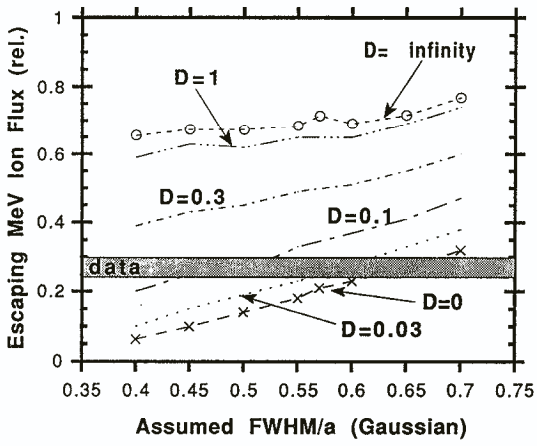

FIG. 19. Calculated flux versus assumed MeV ion source profile width FWHM/a for the 1.8 MA case of Fig. 18. For low values of D the predicted flux varies strongly with the assumed FWHM/a, but at high values of D the predicted flux is roughly independent of D (since all ions are lost). The approximate uncertainty in the SNAP profile value of FWHM/a = 0.57 (also shown) is ±10%.

for the D > 0 curves are not indicated explicitly. The effects of uncertainty in the MeV ion source profile for the 1.8 MA case is illustrated in Fig. 19. There, the SNAP magnetics (from shot #55164) was used in all cases for the plasma current and the Shafranov shift, but the MeV ion source profile was parametrized as a variable Gaussian with a FWHM varied over the range FWHM/a = 0.4–0.7 (the SNAP source profile had FWHM/a = 0.57, also indicated). The same analysis as described above for first-orbit loss, Ω and diffusive loss was repeated for each FWHM value indicated in Fig. 19.

The resulting predicted normalized first-orbit losses (D = 0) varied considerably, e.g. from 0.1 to 0.27 for FWHM/a = 0.45–0.65 (compared to the SNAP profile prediction of 0.21 for FWHM/a = 0.57). However, the predictions for D → ∞ varied by only about 5% over this FWHM variation, because of the approximate invariance of the *total* ion source rate within the detectable region $r < r_{max}$ at a fixed current (for these cases with $r_{fb}/a \gg$ FWHM/2a).

Thus, an experimental uncertainty in the source profile of ±10% [18] gives an estimated uncertainty range of D = 0–0.1 m^2/s for the 1.8 MA case, corresponding to Ω ≈ 2.5 ± 1 within these limits. It should be stressed that the data are consistent with the first-orbit model alone, i.e. D = 0, given the uncertainty in the first-orbit model calculations.

4.6. Pitch angle dependence versus D

The calculated pitch angle dependence for finite D is found by adding to the distributed pitch angle dependence of the first-orbit model the total diffusive flux just at the pitch angle of the fattest banana orbit. The resulting distribution is then smoothed by the detector and the optical resolutions to simulate the experimental results.

Examples of the smoothed diffusive and first-orbit pitch angle distributions are shown in Fig. 20, where

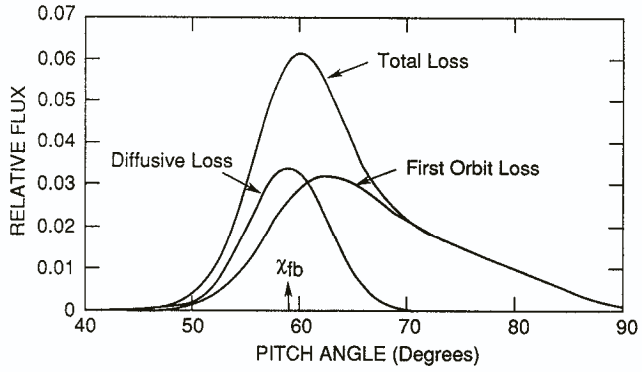

FIG. 20. Examples of calculated pitch angle distributions with and without a contribution from diffusive loss. Both the first-orbit loss curve and the diffusive loss curve were smoothed by the instrumental broadening (≈9° FWHM). The total diffusive loss was assumed to be one half of the total first-orbit loss and was added at χ_{fb}. The total loss curve is narrowed by the presence of diffusive loss.

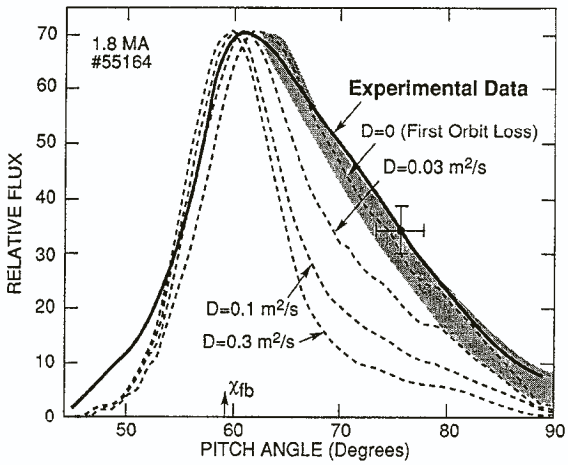

FIG. 21. Measured pitch angle distribution for the 1.8 MA case of Fig. 12 versus the calculated pitch angle distributions for various assumed values of D. Only $D \leq 0.03$ m^2/s is consistent with the data. The error bar shows the approximate shot-to-shot variation, and there is an additional systematic uncertainty of ±3% in the measured pitch angle (not shown). The shaded region shows the uncertainty due to source profile variations for the D = 0 model curve.

for this 1.8 MA case the ratio of the total diffusive flux to the total first-orbit flux was assumed to be 0.5 (corresponding to $D \approx 0.05$ m^2/s). Note that even for this relatively small diffusive contribution the shape of the net pitch distribution narrows significantly. Note also that the symmetric smoothing process shifts the peak of the asymmetric first-orbit distribution slightly from 59° to 62°.

In Fig. 21 the resulting pitch angle distributions versus D are compared with the experimental data from one of the 1.8 MA shots (#55164), where $\Omega = 2.5$ was assumed for all cases. The ratios of the total diffusive loss to the total first-orbit loss were, respectively, 0.3, 0.7 and 1.5 for the assumed $D = 0.03$ m^2/s, 0.1 m^2/s and 0.3 m^2/s. The model distributions for $D \geq 0.1$ m^2/s are all significantly narrower than the experimental distribution, suggesting an upper limit of $D \approx 0.03$ m^2/s in this case. The approximate experimental shot-to-shot flux variation and the uncertainty in the absolute pitch angle are indicated by the error bars on the data (see also Fig. 11).

The uncertainty in this upper limit due to source profile variations can be inferred from the analysis of Fig. 19. For example, with an assumed $D = 0.1$ m^2/s, a variation in the source profile FWHM/a by ±10% from the normal SNAP value gives a ratio of diffusive flux to first-orbit flux of 0.7 ± 0.4, implying that the broadest possible curve (for the larger FWHM) has a shape similar to that for the 0.03 m^2/s case shown in Fig. 21. The uncertainty in the D = 0 analysis due to a ±10% source profile variation is relatively small, as shown by the shaded region in the figure.

Two additional sources of uncertainty are also not represented in Fig. 21. First, the plasma current profile was assumed to be given by the SNAP calculation; in fact, the current profile is not measured, introducing an uncertainty in the pitch angle distribution comparable to that of the source profile [6]. Second, the Gaussian approximation to the instrumental broadening used to smooth the calculated distributions obviously underestimates the actual broadening at $\chi < 50°$ and most likely also does so at $\chi > 70°$. Slightly more broadened model curves would tend to increase the estimated D value inferred from Fig. 21.

Given these uncertainties, an upper limit of $D \approx 0.1$ m^2/s and a lower limit of D = 0 appear to be consistent with the data of Fig. 21.

4.7. Average gyroradius dependence versus D

At the limits $D = 0$ and $D \to \infty$, the value of the escaping MeV ion energy and the gyroradius ρ are expected to be the same as their birth values, since the

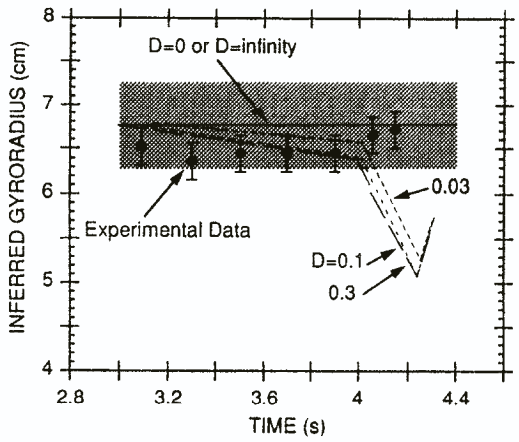

FIG. 22. Measured peak of the gyroradius distribution for the 1.8 MA cases (averaged over the shots in Fig. 13) versus the calculated average gyroradius for various assumed values of D. The measured $\langle\rho\rangle$ does not decrease after NBI, implying that $D \leq 0.03$ m^2/s during this time (or $D \gg 0.3$ m^2/s). The error bars show the shot-to-shot variation of the data, while the dotted region shows the estimated systematic uncertainty in evaluating $\langle\rho\rangle$ from the data. The increase in calculated $\langle\rho\rangle$ at very late times is due to the small remaining first-orbit loss.

loss time in both limits approaches zero. However, for intermediate D, a number of partially thermalized ions will be lost, leading to an expected decrease in the average gyroradius.

Figure 22 shows a plot of the predicted average gyroradius $\langle\rho\rangle$ for various assumed values of D versus time, as evaluated from the energy dependent simulations for 1.8 MA discharges, including the expected decrease in energy after NBI. At the beginning of NBI (at 3.0 s), the predicted gyroradii for all values of D are at the birth value, $\rho = 0.068$ m, since there has not yet been time for diffusing ions to become thermalized. In the steady state phase (at 4.0 s), the calculated $\langle\rho\rangle$ decreases owing to contributions from partially thermalized ions; however, the minimum predicted value is only slightly reduced to $\langle\rho\rangle \approx 0.9\rho$. This approximate invariance of $\langle\rho\rangle$ occurs because, for low D, the average $\langle\rho\rangle$ for diffusing ions is small (e.g. 0.81 for tritons with D $\approx$ 0.03 m^2/s), but the *number* of diffusing ions is much smaller than the number of first-orbit loss ions; conversely, for a high value of D, the number of diffusing ions is large, but their average energy is near to their birth energy because of their short diffusion time. After, NBI the calculated $\langle\rho\rangle$ for D = 0.03–0.3 m^2/s drops rapidly, since the expected first-orbit loss flux decreases much faster than the expected diffusive loss (recall that the neutron decay rate was $\approx$0.06 s, and the triton and proton energy decay times τ_{sE} were 0.6 s and 0.2 s, respectively).

Figure 22 also shows the average of the experimental data points for the four 1.8 MA discharges of Fig. 13, with the error bars corresponding to the relative shot-to-shot variation (the systematic uncertainty in the experimental $\langle\rho\rangle$ of about $\pm$0.01 m is also shown). The experimental average gyroradius did not change at all during the discharge (within the measurement uncertainty), even up to the last visible sign of the escaping MeV ions at 4.15 $\pm$ 0.03 s.

The predicted steady state decreases in $\langle\rho\rangle$ for various values of D are within the experimental error bars; thus no conclusion concerning D can be drawn from steady state measurements. The calculated curves in Fig. 22 after NBI show that the calculated $\langle\rho\rangle$ values for D = 0.03–0.3 m^2/s are significantly below the values obtained at 4.05–4.15 s, even when an uncertainty of about $\pm$0.003 m is included in the calculated $\langle\rho\rangle$ values because of the uncertainty in Ω (2.5 $\pm$ 1).

Taken at face value, this third measurement of escaping MeV ion diffusion seems to confirm the low upper limit of D $\approx$ 0.03 m^2/s, discussed in Sections 4.6 and 4.7. However, in this case there is no way to exclude the possibility that D $\gg$ 0.3 m^2/s, since this limit also implies a negligible change in the average energy after NBI.

4.8. Time dependence versus D

It has been noted that the clearest sign of MeV ion diffusion would be a delayed loss after the turn-off of the MeV ion source, since the time-scale of the diffusive loss may be larger than the time for first-orbit loss to decay away. Examination of the measured time dependences in Section 4.4 (Figs 14–16) shows that the decay rate of the MeV ion signal is very similar to that of the neutron (MeV ion source) signal, implying a relatively small diffusive loss.

Figure 23 shows an example of the predicted loss versus the time after NBI for a 1.8 MA discharge. The expected signals for tritons and protons are shown separately for both the energy independent model (as in Fig. 6) and the final energy dependent model, after correction for the expected energy spectrum (including detector sensitivities). These particular cases, used for

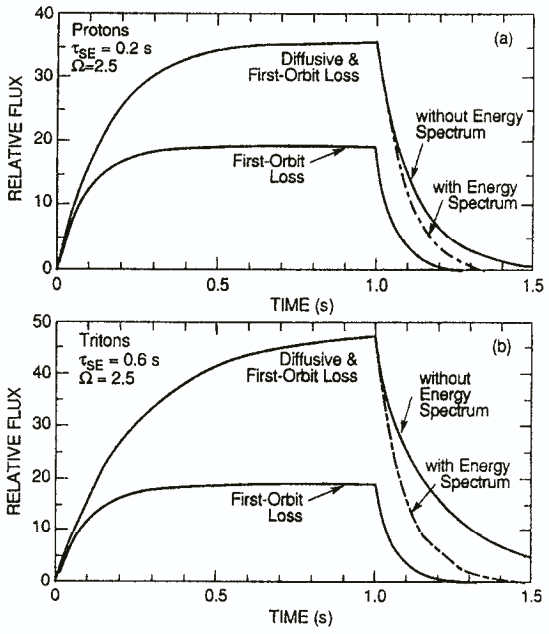

FIG. 23. Calculated time dependences of proton and triton scintillator responses for the 1.8 MA case with and without effects of an energy dependent scintillator response (also compared with the first-orbit loss). When the energy dependent scintillator responses are taken into account, the calculated fluxes decay more rapidly after NBI. Note that the variation in the radius of the passing/trapped boundary with decreasing energy is not taken into account.

illustration, assumed D = 0.1 m^2/s and parameters corresponding to the standard 1.8 MA case, i.e. $r_{fb}/a = 0.52$, $\Omega = 2.5$, $\tau_{sE} = 0.6$ s (tritons), $\tau_{sE} = 0.2$ s (protons) and a first-orbit loss decay time of 0.06 s. Note that uncertainties in τ_{sE} would be related linearly to uncertainty in D, since the shape of these curves for a given Ω vary only with the dimensionless parameter $(D\tau_{sE})^{1/2}/r_{fb}$.

The expected time dependences after NBI as shown in Fig. 23 change significantly when the energy spectrum is taken into account. With the energy spectrum correction, the expected triton signal after NBI e-folds in about 0.1 s (including first-orbit loss), in contrast to the simpler energy independent model, which e-folds in about 0.2 s. This is due to the decay of the energy versus time after NBI (Eq. (22)) of about 10% per 0.06 s (for an energy e-folding time of $\tau_s = 0.6$ s). This reduced light flux is due to the reduced scintillator sensitivity at lower energy, as shown in Fig. 3. For protons, the expected signal after NBI also e-folds over about 0.1 s, but this is not much different from the energy independent model because of the relatively flatter scintillator energy response curve for protons.

Energy dependent calculations such as those shown in Fig. 23 were summed over tritons and protons for various assumed values of D. To display most clearly the effect of finite D on the time dependence after NBI, the ratio between these curves and the expected first-orbit loss after NBI was calculated for each value of D, as shown in Fig. 24. In this case, the diffusive loss causes this ratio to become >1. Note that the first-orbit loss was assumed to decrease with an e-folding time of 0.06 s in all cases, corresponding to the observed neutron decay rate after NBI.

The predicted flux ratios for various values of D are compared with the experimental data in Fig. 24. The experimental points were found by normalizing the measured total MeV ion flux versus time (averaged over all 1.8 MA cases) to the measured neutron rate versus time. For example, with an assumed D = 0.1 m^2/s, the expected MeV ion flux 0.15 s after NBI is about two times the flux expected from first-orbit loss alone, while the measured MeV ion flux at this time is within 1.2 ± 0.1 of the value expected for first-orbit loss alone.

Therefore, this fourth and last analysis again implies an upper limit of D $\approx$ 0.03 m^2/s for MeV ion diffusion during the period 0.05–0.15 s after NBI. However, the same data are also consistent with a very large diffusion, D $\geq$ 1.0 m^2/s (not shown), since at that level the diffusive loss time is less than the decay time for first-orbit loss. In addition, this analysis of the post-NBI phase should be considered to be somewhat tentative until a satisfactory explanation of the apparently delayed rise of the MeV ion loss at the start of NBI is found (see Section 4.4).

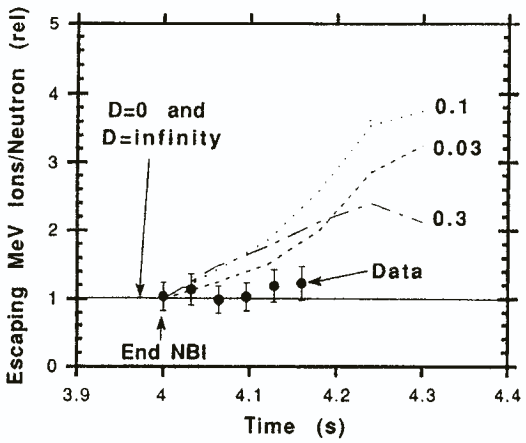

FIG. 24. Calculated versus measured time dependence of the MeV ion flux after NBI for the 1.8 MA case, both normalized by the expected time dependence of the first-orbit loss (neutron decay rate). The models for D = 0.03–0.3 m^2/s predict an increased flux in the period 4.05–4.15 s which is not seen in the data; however, this analysis does not exclude D $\gg$ 0.3 m^2/s.

5. DISCUSSION

Some theory relevant for the present experimental results is outlined in Section 5.1. Section 5.2 is a brief survey of other possible MeV ion loss mechanisms which were not investigated in the present experiment.

5.1. Theoretically predicted MeV ion diffusion coefficients

For a general and accurate evaluation of the neoclassical transport rate for energetic ions, it is necessary to include both pitch angle and slowing down collision effects [15, 21–23]. By retaining both types of collision, Ref. [15] found an enhancement of the neoclassical transport rate over the previous rates, i.e. approximately

$$D_{nc} \approx (r/R)(\rho_{pol})^2/\tau_v \qquad (23)$$

where the velocity slowing down time τ_v has been used. Using $r/R \approx 0.2$, $\tau_v \approx 0.8$ s ($\approx 2\tau_s$ for the high energy ions of interest, in which ion drag is negligible), and

an average poloidal gyroradius $\rho_{pol} \approx 0.4$ m for 1 MeV tritons (or 3 MeV protons) at a plasma current of 1.8 MA, we obtain

$$D_{nc} \approx 0.04 \text{ m}^2/\text{s} \quad (24)$$

Thus, the neoclassical diffusion rate for energetic ions is consistent with the upper limit $D \approx 0.1$ m^2/s inferred from this experiment. Improvements in the modelling and experiment could potentially isolate this neoclassical effect (see Section 5.3).

As mentioned in the introduction, a generalized model for high energy test particle diffusion within a spectrum of small scale magnetic or electrostatic turbulence [7, 14] predicts that fast ions will diffuse more slowly than thermal ions. The analytical theory has been evaluated for a typical high current case in TFTR by Duvall [7], with the very low value of D_{MeV} quoted in Section 1.3.

From another perspective, since the orbit averaging factor Λ of Eq. (1) scales approximately as E^{-1} in the limit $k_\perp \rho_{MeV} \gg 1$, the diffusion rate of 1 MeV tritons should be about 10^{-2} times the diffusion rate of 10 keV thermal ions of $D_i \approx \chi_i \approx 1$ m^2/s, i.e. the MeV ion diffusion rate should be less than 0.01 m^2/s. Thus, the measured upper limit of $D \approx 0.1$ m^2/s was considerably above the MeV ion diffusion rate expected from small scale scale turbulence for this model.

5.2. Other possible loss mechanisms

Before concluding that MeV ion loss is generally small, it is important to note several other possible loss mechanisms which were not measured in the present experiment. Other known MeV ion loss mechanisms in TFTR are associated with sawteeth, coherent MHD and TF ripple loss.

In fact, there were fairly large sawteeth in the 1.8 MA and 2.0 MA discharges described here, with typically two 'crash' times (indicated by the arrows in Fig. 14). As observed previously [24], these sawteeth had little effect on the MeV ion loss to the bottom detector, causing only a transient (<1 ms) increase at the sawtooth crash without much change in the baseline loss level. This is somewhat surprising, since the integrated MeV ion loss over a crash is much less than would be expected if a substantial fraction of the confined ions were lost.

Large coherent MHD oscillations were avoided in the present experiment by operating at moderate beam power and moderate q(a). Previous observations of this mechanism [6, 20, 24] showed sudden *increases* in MeV ion loss correlated with *decreases* in the neutron rate itself (presumably due to anomalous beam ion transport). This type of process did not occur in the discharges analysed in this paper. Several relevant test particle analyses of the effect of MHD activity on fast ions have been performed recently [7, 25–27].

Toroidal field ripple diffusion should affect only trapped particles and so should not be observable as an increased D for the counter-passing ions measured here. Model calculations indicate that this loss should be localized near the outer midplane [28]. In TFTR, separate experiments are in progress to measure this loss there [29].

Note that in some other TFTR discharges (not discussed in this paper) there were significant losses which may not be explainable by any of the mechanisms described so far. For example, one type of anomalous loss sometimes occurred for R = 2.45 m plasmas when a *second* peak in the 2-D scintillator pattern appeared at unexpectedly large χ and small ρ, often modulated by MHD activity. Another anomaly was observed in plasmas with *very* small major radius (R = 2.25 m), which had an anomalously large escaping alpha flux to the bottom detector, as described previously [6]. A third anomaly was observed at very high beam power (>25 MW), when the loss sometimes appeared to increase even without large coherent MHD activity.

All of these MeV ions loss mechanisms need to be investigated further in order to understand alpha particle confinement in D–T plasmas.

6. CONCLUSIONS

Four different experimental measurements of the escaping MeV ion flux from TFTR were examined for possible signs of diffusive loss of internally confined counter-passing ions. In all cases, the results agreed (to within plausible error bars) with the predictions of the simple first-orbit loss model, i.e. there was no clearly measurable MeV ion diffusion. Given the uncertainties in the experiment and the analysis, an upper limit of $D \approx 0.1$ m^2/s was determined from the data and modelling.

Strictly speaking, these results were obtained only for a small class of counter-passing ions with a particular magnetic moment ($\mu/\mu_0 \approx 0.6$) in the interior ($r/a < 0.5$) of TFTR discharges with 1.4–1.8 MA and $R_0 = 2.6$ m at moderate power (<16 MW). However, it is plausible that most of the *passing* ions have a similar behaviour, since there is no reason to suppose that the background plasma turbulence would be specially resonant with any particular (r, μ) subset of these passing MeV ions. The

diffusion coefficients obtained in the present study are also similar to those inferred in different ways for other fast ion populations in tokamaks [9–13]; in particular, a recent analysis of the radial profile of triton burnup in JET implied an even lower value, $D \approx 0.01$ m^2/s [30].

The inferred MeV ion diffusion rate of $D \leq 0.1$ m^2/s is well below the thermal ion heat and particle diffusivities of $D \approx 1$ m^2/s for $r/a \approx 0.3$–0.5 for the same 1.8 MA plasmas. This is most probably due to the theoretically predicted 'orbit averaging' effect, which reduces substantially the expected diffusion for these large gyroradius MeV ions in a background spectrum of small scale turbulence (Section 5.1).

For alpha particle heating of a fusion reactor, the loss due to diffusion of MeV ions at a rate of $D \approx 0.1$ m^2/s would not be a problem, since the loss time would be much longer than the thermalization time; for example, for ITER, $\tau_{loss} \approx a^2/4D \approx 10$ s $\gg \tau_{\alpha,therm} \approx 1$ s. Because of the narrow banana widths at these high plasma currents the first-orbit loss will be negligible and MeV ions would have to diffuse almost to the plasma edge before being lost across the passing/trapped boundary.

In any attempts to further improve the precision of this experimental upper bound of D to below $D \approx 0.1$ m^2/s, several other processes should be incorporated in the modelling. First, it is plausible that D has a tendency to be maximum near the passing/trapped boundary (where the orbital stagnation occurs and where the detector measures the loss), so that the inferred upper bound may actually be an *overestimate* of D for MeV ions in the bulk of the region $r < r_{fb}$. Second, the possibility of pitch angle scattering in μ/μ_0 'vertically' across the passing/trapped boundary (e.g. neoclassical diffusion) should be explicitly taken into account, which would also tend to reduce the spatial diffusion rate inferred for a given experimental result. Third, the systematic increase in r_{fb}/a with decreasing energy should also be included, which would tend to decrease the expected flux and to increase the inferred diffusion rate below $D \approx 0.1$ m^2/s (r_{fb}/a typically increases from ≈ 0.3 at E_0 to ≈ 0.4 at $E_0/2$). Finally, a fully time dependent and energy dependent model is needed to check the simplified energy dependent modelling discussed in this paper. Recently, an independent confirmation of the basic modelling results of Section 3.7 was obtained using a code to calculate $f(r, E, t)$ [31].

It is important to note that this experiment did not address several other possible MeV ion loss mechanisms, for example those affecting *trapped* ions (e.g. ripple) or those associated with large scale coherent MHD or sawteeth. In particular, we have not simulated the behaviour of alpha particles during D–T experiments, when alpha driven MHD effects may become dominant. However, a repetition of the same experiment during the D–T phase of TFTR could resolve some of these open questions with respect to the confinement of D–T alpha particles.

ACKNOWLEDGEMENTS

The authors thank C.W. Barnes, R.E. Duvall, R.J. Goldston, L. Johnson, K. McGuire, D. Meade, D. Monticello, J. Schivell, S. Scott, J.D. Strachan, R.B. White, K.M. Young for various contributions to this project.

The work was supported by the United States Department of Energy, under Contract No. DE-AE02-76-CHO3073.

REFERENCES

[1] FURTH, H.P., GOLDSTON, R.J., ZWEBEN, S.J., SIGMAR, D.J., Nucl. Fusion **30** (1990) 1799.
[2] KOLESNICHENKO, Ya.I., SIGMAR, D.J., Nucl. Fusion **30** (1990) 777.
[3] WHITE, R.B., MYNICK, H.E., Phys. Fluids B **1** (1989) 980.
[4] GOLDSTON, R.J., WHITE, R.B., BOOZER, A.H., Phys. Rev. Lett. **47** (1983) 647.
[5] TANI, K., TAKIZUKA, T., AZUMI, M., KISHIMOTO, H., Nucl. Fusion **23** (1983) 657.
[6] ZWEBEN, S.J., BOIVIN, R.L., DIESSO, M., et al., Nucl. Fusion **30** (1990) 1551.
[7] DUVALL, R.E., Topics in Action-Angle Methods Applied to Tokamak Transport, PhD Thesis, Princeton University, Princeton, NJ (1990).
[8] BATISTONI, P., BARNES, C.W., Computation of Classical Triton Burnup with High Plasma Temperature and Current, Rep. PPPL-2706, Princeton Plasma Physics Laboratory, Princeton University, Princeton, NJ (1990).
[9] SCOTT, S.D., BARNES, C.W., GRISHAM, L.R., et al., in Plasma Physics and Controlled Nuclear Fusion Research 1990 (Proc. 13th Int. Conf. Washington, DC, 1990), Vol. 1, IAEA, Vienna (1991) 235.
[10] SADLER, G.J., CONROY, S.W., JARVIS, O.W., et al., Fusion Technol. **18** (1990) 556.
[11] COTTRELL, G.A., START, D.F.H., Nucl. Fusion **31** (1991) 61.
[12] RADEZTSKY, R.H., SCOTT, S.D., KAITA, R., et al., in Controlled Fusion and Plasma Heating (Proc. 15th Eur. Conf. Dubrovnik, 1988), Vol. 12B, Part I, European Physical Society (1988) 79.

[13] HAWRYLUK, R.J., ARUNASALAM, V., BARNES, C.W., et al., Overview of TFTR Transport Studies, Rep. PPPL-2783, Princeton Plasma Physics Laboratory, Princeton University, Princeton, NJ (1991).
[14] MYNICK, H.E., DUVALL, R.E., Phys. Fluids B **1** (1989) 750; MYNICK, H.E., KROMMES, J.A., Phys. Fluids **23** (1980) 1229.
[15] HSU, C.T., CATTO, P.J., SIGMAR, D.J., Phys. Fluids B **2** (1990) 280.
[16] FELT, J., BARNES, C.W., CHRIEN, R.E., et al., Rev. Sci. Instrum. **61** (1990) 3262.
[17] BOIVIN, R., Measurements of Charged Fusion Product Diffusion in TFTR, PhD Thesis, Princeton University, Princeton, NJ (1991); Rep. PPPL-2797, Princeton Plasma Physics Laboratory, Princeton University, Princeton, NJ (1990).
[18] ZWEBEN, S.J., BOIVIN, R., CHANG, C.S., HAMMETT, G., MYNICK, H.E., Search for Diffusion of Counter-Passing MeV Ions in the TFTR Tokamak Rep. PPPL-2770, Princeton Plasma Physics Laboratory, Princeton University, Princeton, NJ (1991).
[19] JOHNSON, L. (PPPL), personal communication, 1991.
[20] ZWEBEN, S.J., BOIVIN, R.L., DUVALL, R.E., et al., Phys. Fluids B **2** (1990) 1411.
[21] YAVORSKIJ, V.A., YAKOVENKO, Yu.V., in Controlled Fusion and Plasma Heating (Proc. 17th Eur. Conf. Amsterdam, 1990), Vol. 14B, Part II, European Physical Society (1990) 699.
[22] NOCENTINI, A., TESSAROTTO, M., ENGELMANN, F., Nucl. Fusion **15** (1975) 359.
[23] CHANG, C.S., HAMMETT, G.W., GOLDSTON, R.J., Phys. Fluids B **2** (1990) 2382.
[24] ZWEBEN, S.J., STRACHAN, J.D., BOIVIN, R., et al., in Controlled Fusion and Plasma Physics (Proc. 16th Eur. Conf. Venice, 1989), Vol. 13B, Part I, European Physical Society (1989) 39.
[25] HSU, C.T., SIGMAR, D.J. (MIT, Cambridge), personal communication, 1991.
[26] KONOVALOV, S.V., PUTVINSKY, S.V., Fusion Technol. **18** (1990) 397.
[27] BITTONI, E., HAEGI, M., Alpha particle confinement in the presence of magnetic ripple and MHD perturbations, paper presented at IAEA Workshop on Alpha Particle Effects in Fusion Devices, Stockholm, 1991.
[28] GOLOBOROD'KO, V.Ya., YAVORSKIJ, V.A., Nucl. Fusion **29** (1989) 1025.
[29] BOIVIN, R., KILPATRICK, S., MANOS, D., ZWEBEN, S., Rev. Sci. Instrum. **61** (1990) 3206.
[30] JARVIS, O.N., ADAMS, J.M., CONROY, S.W., et al., in Controlled Fusion and Plasma Physics (Proc. 18th Eur. Conf. Berlin, 1991), Vol. 15C, Part I, European Physical Society (1991) 21.
[31] SCHIVELL, J. (PPPL), personal communication, 1991.

(Manuscript received 16 May 1991
Final manuscript received 17 September 1991)